A review of orbital-scale monsoon variability and dynamics in East Asia during the Quaternary

Youbin Sun[a, b, *], Ting Wang[a, c], Qiuzhen Yin[d], Anqi Lyu[d], Michel Crucifix[d], Yanjun Cai[e], Li Ai[a], Steven Clemens[f], Zhisheng An[a,b,g]

[a] State Key Laboratory of Loess and Quaternary Geology, Institute of Earth Environment, Chinese Academy of Sciences, Xi'an, China

[b] Center for Excellence in Quaternary Science and Global Change, Chinese Academy of Sciences, Xi'an, China

[c] College of Earth Science, University of Chinese Academy of Sciences, Beijing, China

[d] Georges Lemaître Center for Earth and Climate Research, Earth and Life Institute, Université catholique de Louvain, Louvain-la-Neuve, Belgium

[e] Institute of Global Environmental Change, Xi'an Jiaotong University, Xi'an, China

[f] Department of Earth, Environmental and Planetary Sciences, Brown University, Providence, USA

[g] Open Studio for Oceanic-Continental Climate and Environment Changes, Pilot National Laboratory for Marine Science and Technology, Qingdao, China

* Corresponding to Youbin Sun (sunyb@ieecas.cn)

Abstract： Quaternary monsoon changes in East Asia have been extensively investigated using proxy records from continental and marine archives. However, these proxy indicators show different characteristics in terms of trends and rhythms, resulting in controversial understanding of orbital-scale monsoon dynamics. Here we review the orbital-scale monsoon variability and dynamics in East Asia by comparing multiple proxies from loess, lake, speleothem, and marine records with the HadCM3 modeling result. Wavelet spectra of representative records reveal that changes in winter monsoon and sea surface temperature exhibit a remarkable shift from 41- to 100-kyr cycles across the mid-Pleistocene transition (MPT), whereas other proxy records (e.g. $\delta^{13}C$ of loess carbonate, pollen concentration in lake sediments, and magnetic mineral compositions in marine sediment) display strong and persistent precession cycles through the Quaternary, along with distinct 100-kyr cycles after the MPT. Simulations with the HadCM3 climate model reveal that the effects of orbital parameters, ice volume, and CO_2 concentration on the temperature, precipitation, and southerly winds are spatially different in East Asia. Orbitally induced insolation plays a dominant role in driving changes in summer temperature and southerly wind, while ice volume and CO_2 play different roles in affecting annual precipitation and temperature. The effects of insolation and ice/CO_2 on the summer precipitation are significantly different between northern and southern China. Proxy-model comparison suggests that several land-based proxies are sensitive to changes in summer precipitation, annual precipitation, and annual temperature, respectively, though their responses to astronomical, ice, and CO_2 forcing being quite different. Our proxy-model comparison reveals that complex expression of Quaternary climate periodicities was provoked by different sensitivities of marine and terrestrial proxies to changes in precipitation and temperature, and by different responses of temperature and precipitation to insolation and ice/CO_2 forcing. We suggest that mechanisms of Quaternary climate change can be deepened by further comparison of quantitatively reconstructed paleotemperature and precipitation data with climate variables from high-resolution regional Earth climate system models.

Keywords: East Asia; Quaternary monsoon change; Proxy records; Modeling results; Orbital-scale monsoon dynamics.

1. Introduction

Milutin Milankovitch proposed that changes in orbitally-induced summer insolation played a key role in driving glacial cycles (Milankovitch, 1941), which was subsequently the basis of what is now termed the "Milankovitch theory" (Hays et al., 1976; Imbrie and Imbrie, 1979; Berger et al., 1984). The theory suggests that ice/snow melting during the summer season, induced by incoming solar radiation in the Northern Hemisphere high-latitude region, is a driver or at least a pacemaker of the Quaternary ice-age cycles. Benthic $\delta^{18}O$ records from deep-sea sediments have provided robust evidence supporting the Milankovitch theory (Hays et al., 1976; Shackleton and Opdyke, 1976). Spectral analysis of the 2-Myr $\delta^{18}O$ record reveals a notable periodicity shift from 41-kyr before ~1.2 Ma to 100-kyr after ~0.8 Ma (Pisias and Moore, 1981), which has been named the Mid-Pleistocene transition (MPT) (e.g. Ruddiman et al., 1986; Raymo et al., 1997; Clark et al., 2006). Over the past three decades, numerous proxies from deep-sea sediments reveal that changes in global ice volume (e.g. Lisiecki and Raymo, 2005), sea level (Rohling et al., 2014), sea surface temperature (Elderfield et al., 2012), and thermohaline circulation (Raymo et al., 1997) all exhibit a periodicity shift from 40 kyr to 100 kyr cycles across the MPT (e.g. Clark et al., 2006; Head and Gibbard, 2015).

In contrast to the marine-based MPT characteristics, many records from the global monsoon domain exhibit strong precession cycles during the mid-to-late Pleistocene (e.g. Wang et al., 2014; An et al., 2015). In the Asian monsoon region, the precession signal is quite evident in Chinese speleothem and Arabian sea sediments (e.g. Wang et al., 2008; Ziegler et al., 2010; Cayley et al., 2011; Cheng et al., 2016), with the monsoon responses to astronomical and glacial forcing being recognized in Chinese loess and marine sediments (e.g. Liu et al., 1999; Ding et al., 2002b; Wang et al., 2003; Sun et al., 2006a, 2015; Maher, 2016; Clemens et al., 2008, 2018). Most notably, absolutely-dated speleothem $\delta^{18}O$ records in East Asia exhibit prominent 23-kyr precession cycles over the past 640 ka (Wang et al., 2008; Cheng et al., 2016). Hydrologically-related proxies from paleolakes in the Tengger desert, Heqing and Zoige basins and $\delta^{13}C$ of inorganic carbonate from Jingyuan loess sequence all exhibit strong precession cycles through the Pleistocene (An et al., 2011; Sun et al., 2019; Zhao et al., 2020; Liu et al., 2021). However, precessional cycles are absent in the seawater $\delta^{18}O$-based runoff reconstruction from the East China Sea (Clemens et al., 2018). Aside from the precession signal, 100-kyr cycles are found in loess grain-size (e.g. Ding et al., 1994,

2002a; Sun et al., 2006a, 2006b) and planktonic $\delta^{18}O$ and elemental ratios from the marginal sea sediments (e.g. Wang et al., 2003; Clemens et al., 2008, 2018; Yao et al., 2012; Kunkelova et al., 2018), implying that Northern Hemisphere ice sheet (NHIS) also plays a key role in driving glacial-interglacial monsoon variations.

Climate change in East Asia, including the eastern and southern Asian continent, and the surrounding oceans (e.g. East China Sea, South China Sea, Arabian Sea, Bay of Bengal), is affected by both low-level Asian monsoon circulation and high-level Northern Hemisphere westerly jet (Gao et al., 1962; Ding and Chan, 2005) (Fig.1). The Asian monsoon consists of the East Asian monsoon (EAM) and the Indian summer monsoon (ISM) (Wang, 2006). Over past decades, many proxy records from four representative archives (i.e. loess, stalagmites, desert, lake and marine sediments) have been extensively investigated to reconstruct monsoon-induced changes in wind and precipitation during the Quaternary (e.g. Liu and Ding, 1998; An, 2000; Wang et al., 2005; An et al., 2012; Chen et al., 2019; Liu et al., 2021). Notably, these proxies exhibit quite different characteristics in terms of trends (weakening vs. strengthening of the monsoon intensity) and rhythms (100- vs. 23-kyr cycles) (e.g. Liu et al., 1999; Sun et al., 2006a; Wang et al., 2008; Wang et al., 2014; An et al., 2015; Cheng et al., 2016), resulting in diverse manifestation of orbital-scale monsoon variability (e.g. Clemens et al., 1991; Ding et al., 1995; An et al., 1991, 2011; Wang et al., 2017; Cheng et al., 2021).

Dynamically, drivers of orbital-scale climate changes include external forcing of three astronomical parameters (Berger, 1978), internal factors of changing ice-sheets on both hemispheres (Zachos et al., 2001), and atmospheric concentrations of greenhouse gases (Petit et al., 1999). Numerical simulations with general circulation models have long been performed to understand relative impacts of these forcing factors on orbital-scale monsoon variability (e.g. Kutzbach and Otto-Bliesner, 1982; Kutzbach et al., 2008). Sensitivity experiments generally suggest that astronomical parameters, ice sheet, and atmospheric CO_2 concentrations all affect orbital-scale monsoon variability (Prell and Kutzbach, 1987, 1992; Yin et al., 2009; Lu et al., 2013; Liu et al., 2014). Transient simulations reveal that the impacts of insolation, ice and CO_2 on summer precipitation and southerly wind changes since the last glacial maximum are spatially different in the East Asian continent (Liu et al., 2014; Wen et al., 2016). Other simulations show that the specific responses of summer monsoon to ice, CO_2 and astronomical are regionally dependent (Yin et al., 2008, 2009; Araya–Melo et al., 2015; Sun et al., 2019; Lyu et al., 2021). Clearly, regional different responses of the precipitation

and wind changes to external and internal forcing can also lead to controversial understanding of orbital-scale monsoon dynamics (Liu et al., 2014; Cheng el., 2021).

Proxy-model comparisons, while largely limited to last several climate cycles (e.g. Yin et al., 2008; Shi et al., 2011; Lu et al., 2013; Liu et al., 2014; Sun et al., 2015), have already provided valuable insights into orbital-scale monsoon dynamics. In this review, we extend proxy-data comparison back to the Quaternary by comparing multiple proxy records from four archives in East Asia with the HadCM3 modeling results (i.e. temperature, wind and precipitation). The main objective is to address the spatiotemporal characteristics of Quaternary climate change in East Asia (mainly the EAM and ISM) and its underlying dynamics. In Section 2, multiple proxy records from loess, cave, lake, and deep-sea sediments are synthesized as reflecting changes in ice volume, temperature, wind intensity, monsoon-induced hydrological and weathering processes. In Section 3, representative proxies are chosen to address the spatiotemporal features of Quaternary climate variations. Evolutionary power spectra of these sensitive proxies are then applied to assess the Quaternary evolution of dominant climatic periodicities. In Section 4, simulated changes in temperature, precipitation, and southerly wind are presented to address the spatial expressions of the climate response to astronomical, and ice/CO_2 forcing. Finally, proxies and model results are directly compared to infer the characteristics and dynamics of Quaternary climate changes in the East Asian monsoon-affected region.

2. Archives and proxies

Over the past three decades, more than sixty sites in East Asia and proximal oceans have been studied to address Quaternary climate fluctuations associated with changes in EAM and ISM (Fig.1). Quaternary climate changes in the larger Asian monsoon domain were initially investigated using Chinese loess sequences and marine cores retrieved by the Ocean Drilling Program (ODP) from the Arabian Sea, the Japan Sea, and the South China Sea (e.g. An et al., 1990; Clemens et al., 1991; Tada et al., 1992; Wang et al., 2003). Subsequently, many loess sequences on the Chinese Loess Plateau have been studied to reconstruct Quaternary monsoon changes (e.g. An et al., 1990; Chen et al. 1991; Xiao and An, 1999; An, 2000; Ding et al., 2002; Sun et al., 2006a, 2019, 2021; Zhang et al., 2016; Fang et al., 2020) (Fig. 1b and Table 1). In addition, eolian-larcustrine sediments in Northern Chinese deserts (Li et al., 2014, 2017; Wang et al., 2015; Liu et al., 2021), Lake Qinghai (Fu et al., 2013), and Lake Luyanghu

(Rits et al., 2016) have also been investigated to reflect Quaternary environmental changes associated with East Asian monsoon circulations. Meanwhile, long-term records of ISM changes have been derived from lake sediments from Cuoe (Lü et al., 2001), Heqing (HQ, An et al., 2011), and Zoige Basin (ZB, Zhao et al., 2020).

Sediments in the coastal zone and marginal seas have also been used to reconstruct Quaternary changes in sea level and monsoonal precipitation (e.g. Yao et al., 2012; Yi et al., 2016; Liu et al., 2016). Recent monsoon cruises conducted by the Integrated Ocean Drilling Program (IODP) have drilled a number of sites in the Japan and East China Seas (e.g. Tada et al., 2018; Irino et al., 2018), South China Sea (e.g. Miao et al., 2017; Gai et al., 2020), Bay of Bengal (Clemens et al., 2016, 2021; France-Lanord et al., 2016), and Arabian Sea (e.g. Betzler et al., 2018; Kunkelova et al., 2018; Pandey et al., 2016). Multiple proxies from these marine cores have been employed to reflect monsoon-induced changes in chemical weathering, paleoproductivity, detrital influx, sea surface salinity and temperature (Wang et al., 2005, also see a brief summary of these marine archives and proxies in Table 1). Unlike the widely distributed Quaternary loess, lake, and marine sediments, absolutely dated speleothem records mainly span the last 640 ka (e.g. Wang et al., 2008; Cai et al., 2015; Cheng et al., 2012, 2016).

The Asian monsoon is driven by the land-ocean thermal gradient and cross-equatorial pressure gradient over the Asian-Indian-Pacific region (Webster et al., 1998; Ding and Chan, 2005; Wang and Ding, 2008; Geen et al., 2020). The geographic location of the East Asian continent and its surrounding oceans conveniently allows for a detailed land-ocean comparison and further exploration of the dynamics and characteristics of Quaternary monsoon change. Here four loess sequences (Jingyuan, Luochuan, Xifeng and Lingtai) and two marine records (ODP sites 1143 and 1146) are chosen to asses Quaternary EAM change, and two lake records (Zoige, and Heqing) are selected to infer ISM variability (see red labels in Fig.1). These records were chosen due to their long duration (>1.5 Myr), millennial resolution (<4 kyr), well constrained age models, and availability of multiple proxies sensitive to orbital-scale monsoon change. In addition, speleothem $\delta^{18}O$ records for Hulu and Sanbao caves are compared to assess orbital-scale monsoon changes over the last 640 kyr (Wang et al., 2001, 2008; Cheng et al., 2016).

2.1. Loess sequences

Chinese has been investigated as a unique continental archive to reconstruct glacial-

interglacial fluctuations of the East Asian monsoon since the 1990s (e.g. An et al., 1990; Ding et al., 1995; Liu and Ding, 1998; An, 2000; Maher, 2016). Three classic loess profiles (Xifeng, Lingtai, Luochuan) in the central Chinese Loess Plateau (CLP) and one high-sedimentation-rate loess sequence (Jingyuan) from the northwestern CLP are selected for addressing orbital-scale fluctuations of the East Asian monsoon during the Quaternary. Grain size parameters (e.g. mean, median, and coarse fraction) of loess deposits have been widely employed to reflect the strength of dust transport dynamics, e.g., coarser grain-size reflecting stronger winter monsoon (An et al., 1991a; Xiao et al., 1992; Ding et al., 2002; Lu et al., 2004; Sun et al., 2006a; Hao et al., 2012). Mean grain-size results of three loess-paleosol sequences on the central CLP exhibit significant glacial-interglacial fluctuations spanning the last 2.6 Myr (Fig.2a and b, Sun et al., 2006a; Han et al., 2020). By contrast, Jingyuan loess sequence from the northwestern CLP usually exhibits much stronger glacial-interglacial variation and persistent millennial-scale oscillations, due to its proximal to the northern Chinese deserts (Fig.2c, Sun et al., 2019).

Magnetic susceptibility (MS) has been widely used to infer the summer monsoon intensity since strong pedogenesis leads to enhanced formation of secondary magnetic minerals (Zhou et al., 1990; An et al., 1991b; Maher and Thompson, 1995). MS records from the central CLP exhibit large amplitude fluctuations (e.g. An et al., 1990; Xiao and An, 1999; Lu et al., 1999; Sun et al., 2006a), corresponding well to the glacial-interglacial alternations between loess and paleosol layers (Fig.2c and d). In contrast, MS variation at Jingyuan profile is very sensitive to interglacial climate changes and exhibit precession-scale variations during the last three interglacials (Fig.2f, Sun et al., 2019). In addition to the widely employed MS proxy, the $\delta^{13}C$ records of inorganic carbonate in loess sediments have been proposed as sensitive proxies for precipitation-induced vegetation change (Liu et al., 2011; Yang et al., 2015). A 1.7-Myr $\delta^{13}C$ record of loess carbonate at Jingyuan section exhibits a different cyclic shift from a dominant 23-kyr cycle before 1.2 Ma to combined periodicities at 100, 41, and 23-kyr bands (Fig.2g, Sun et al., 2019). Unlike evident glacial-interglacial cycles in most loess proxies, the Sr/Ca ratio of microcodium in Chinese loess (a novel proxy for precipitation, Li and Li, 2014) as an unique exception demonstrates persistent obliquity cycles through the Pleistocene (Li et al., 2016).

2.2. Lake sediments

Lake sediments are valuable for providing hydrological and weathering records of the

lake catchments, which are greatly influenced by both regional and global climate changes (Williams et al., 2001; An et al., 2011). Two lake records from the Heqing (HQ) (An et al., 2011) and Zoige Basin (ZB, Zhao et al., 2020) are selected to address orbital-scale ISM change. Paleolake HQ located in southwestern China is greatly influenced by the ISM change, characterized by warm wet summer and cool dry winter (Shen et al., 2007; An et al., 2011). *Tsuga* flourishes under moderately warm and humid conditions and therefore higher *Tsuga* content corresponds to warmer interglacial periods in Heqing record (Fig.3a). The total organic carbon (TOC) content in the lacustrine sediments is closely correlated to ISM-induced changes in catchment biomass and lake productivity, capturing the strong monsoon events during interglacials (Fig.3b). The Rb/Sr ratio reflects the weathering intensity within the catchment area, sensitive to weak monsoon events during glacial times (Fig.3c). Thus, a stacked Rb/Sr and TOC (ISM index) from Lake Heqing is employed as a reliable proxy reflecting the full amplitude of glacial-interglacial ISM variability (Fig.3d). The Zoige Basin located on the eastern Tibetan Plateau is also affected by the ISM climate. In this region, the density and elevation limits of forests are mainly controlled by temperature rather than precipitation, since the moisture availability is plentiful for plant growth (Shen et al., 2005). Therefore, the arboreal pollen abundances (AP%, Fig.3e) from the ZB sediment is regarded as a primary reflection of temperature change (Zhao et al., 2020).

2.3. Deep-sea sediments

After two monsoon-related ODP cruises in the Arabian sea and South China Sea last century (e.g. DeMenocal et al., 1991; Clemens et al., 1991, Wang et al., 2000, 2003), many new marine cores have been recently retrieved from the Japan Sea, East China Sea, and South China Sea, Bay of Bengal, and Arabian Sea in the IODP monsoon cruises (Fig.1 and Table 1, e.g. Clemens et al., 2016; Pandey et al., 2016; Tada et al., 2015, 2018; Betzler et al., 2018). Yet long, high-resolution and multiple proxies sensitive to monsoon changes from these sites are still limited (e.g. Kunkelova et al., 2018; Irino et al., 2018; Clemens et al., 2021). Here we select proxy records of ODP sites 1143 and 1146 in the South China Sea to address their sensitivity to EAM changes. These marine-based proxies can be divided into three types: $\delta^{18}O$ of benthic ($\delta^{18}O_b$) and planktonic ($\delta^{18}O_p$) foraminifera, sea surface temperature (SST), and mineral and chemical indicators. $\delta^{18}O_b$ record has long been regarded as a proxy for changes in global ice volume and deep-water temperature (Shackleton, 2000; Zachos et al., 2001; Elderfield et al., 2012). Comparably, $\delta^{18}O_p$ is regarded as a function of sea surface/sub-surface

temperature, sea level and local salinity (Bemis et al., 1998; Elderfield and Ganssen, 2000; Rohling, 2007). Removal of the temperature and global sea-level effects from $\delta^{18}O_p$ can isolate the sea surface salinity component, which is usually employed to reflect rainfall/runoff change in monsoon-affected area (e.g. the Yangtze River Valley, Clemens et al., 2018). The benthic $\delta^{18}O$ records of ODP sites 1143 and 1146 demonstrate quite similar glacial-interglacial fluctuations (Fig.4a and b). $\delta^{18}O_p$ data obtained from *Globigerinoides* (*G. ruber* and *G. sacculifer*) of ODP site 1143 sites also exhibit similar glacial-interglacial variability (Fig.4c).

SST changes can be inferred from alkenone U^{K}_{37}' index, Mg/Ca ratios, and foraminifera transfer functions. The unsaturation index of alkenones (U^{K}_{37}') produced by coccolithophores is sensitive to the mean annual SST (Müller et al., 1998). Two alkenone-based time series from ODP sites 1143 and 1146 display significant glacial-interglacial SST changes through the Quaternary (Fig.4d and e, Herbert et al., 2010; Li et al., 2011). Mineral and elemental proxies have been used to reconstruct the evolution of the Asian monsoon-induced productivity and chemical weathering in source regions (e.g. Clemens et al., 2008; Zhang et al., 2009; Tian et al., 2011). Since hematite formation is favored by dry conditions whereas goethite is formed under relatively humid conditions (Zhang et al., 2009), the hematite/goethite (Hm/Gt) ratio at ODP Site 1143 is precipitation-dependent and highly sensitive to summer monsoon change (Fig.4f). The Ti/Al is interpreted as an indicator of monsoon-induced weathering intensity (Fig.4g), since Ti is more conservative than Al during chemical weathering processes (Wehausen and Brumsack, 2002; Wei et al., 2006; Tian et al., 2011). Meanwhile, the Ba/Al ratio is often used to infer the monsoon-induced paleoproductivity (Fig.4h), because increased Ba flux is associated with strong winter monsoon and the enhanced nutrient supply owing to strong winter monsoon (Wehausen and Brumsack, 2002; Clemens et al., 2008).

3. Characteristics of Quaternary climate change

3.1. EAM evolution inferred by loess proxies

Proxy records from Chinese loess deposits can well reflect monsoonal wind and precipitation changes (An et al., 1990; Liu and Ding, 1998; Xiao and An, 1999; An, 2000; Ding et al., 2002b; Lu et al., 2004; Sun et al., 2010). East Asian winter monsoon variation, mainly inferred by loess grain-size parameters, exhibit large amplitude fluctuations at glacial-

interglacial time scales (e.g. Ding et al., 1995, 2002a; Xiao and An, 1999; Sun et al., 2006a). Grain-size results of loess deposits assembled herein exhibit a coarsening trend from the early to the mid-late Pleistocene (Fig.2a-c). Remarkable coarsening of two thick silt loess units (L_9 and L_{15}) is evident in Chinese loess sequences, likely related to regional tectonic activities of the northern Tibetan Plateau and/or the Yellow River (Xiao and An, 1999; Sun and Liu, 2000; Li et al., 2014; Han et al., 2014). The amplitude and duration of glacial-interglacial fluctuations of loess grain-size increased significantly during 1.2-0.9 Ma, reflecting the gradual expansion of the NHIS across the MPT (Lisiecki and Raymo, 2005; Clark et al., 2006). Besides sharing similar glacial-interglacial fluctuation, mean grain-size of high-sedimentation-rate loess sequence from the northwestern CLP are characterized by more distinctive precession- and millennial-scale oscillations (Fig.2c, Sun et al., 2019).

The MS variations of three loess sequences from the central CLP exhibit similar glacial-interglacial fluctuations, superimposed by two stepwise increases at palaeosols S_{14} (~1.25 Ma) and S_5 (~0.5 Ma) (Fig.2d and e). However, the MS record at Jingyuan profile exhibits a significant strengthening of the summer monsoon intensity in S_4 (Fig.2f), consistent with the Mid-Brunhes event occurred at the marine isotope stage (MIS) 12/11 boundary (Jansen et al., 1986; Lisiecki and Raymo, 2005; Berger et al., 2016). Due to relatively high sedimentation rates of loess deposits in the western CLP (Sun et al., 2006b, 2019), MS variations of three palaeosol layers (S_1-S_3) exhibit three peaks corresponding to precession-driven insolation cycles. MS records of loess layers in the western CLP are less sensitive to summer monsoon changes since the precipitation is relatively low during glacial periods (Chen et al., 1991; Sun et al., 2006b; Lu et al., 2012; Maher, 2016). By contrast, the carbon isotope of loess carbonates in the northwestern CLP is very sensitive to monsoon-induced vegetation changes (Liu et al., 2011; Sun et al., 2015). A 1.7-Myr $\delta^{13}C$ record of inorganic carbonate ($\delta^{13}C_{IC}$) from JY section exhibits a unique periodicity transition from dominant 21-kyr before 1.2 Ma to combined 100- and 21-kyr cycles after 0.7 Ma (Fig.2g, Sun et al., 2019).

Variations of loess grain-size and MS suggest that the amplitudes of the East Asian winter and summer monsoon increased remarkably after 1.25 Ma, as manifested by simultaneous enhancing of the summer monsoon intensity during interglacials and the winter monsoon strength during glacial periods (Ding et al., 2002; Sun et al., 2006a). Similar long-term trend and cycle-by-cycle correlation of loess grain-size and benthic $\delta^{18}O$ suggest that Quaternary winter monsoon evolution is driven by the waxing and waning of the NHIS (Ding et al., 1995;

Liu et al., 1999). However, the MS records increase remarkably in S_{13} and $S_{5\text{-}1}$ (Fig.2f-h), implying that stepwise strengthening of the summer monsoon during the Quaternary was likely related to the phased uplift of the northeastern Tibetan Plateau around 1.2-0.9 Ma (Sun and Liu, 2000a; Li et al., 2014) and/or the asymmetric developments of bi-polar and Eurasian ice sheets around 0.5 Ma (Yin et al., 2008, 2009; Guo et al., 2009). Unlike the marked MS increase in $S_{5\text{-}1}$ to S_4 (Ding et al., 2002; Sun et al., 2006b; Ao et al., 2020; Sun et al., 2021), the loess $\delta^{13}C_{IC}$ and speleothem $\delta^{18}O$ records exhibit an uniform amplitude during the Mid-Brunhes epoch (Fig.2j and k, Cheng et al., 2016; Sun et al., 2019). Such a discrepancy indicates that prolonged pedogenesis duration of paleosol layers and increased detrital input of magnetic minerals might also affect the enhancing of magnetic susceptibility in Chinese loess (Maher and Thompson, 1995; Sun and Liu, 2000b). Moreover, since the upper and middle reaches of the Yellow River as potential sources of loess deposit have been stepwise expanded during the Quaternary (Nie et al., 2015), provenance shift can potentially complicate interpretation of loess proxy indicators (Zhang et al., 2021),

3.2. ISM variability inferred by lake sediments

The pollen and geochemical records from the sediments of paleolake HQ are presented to infer the ISM variability over the past 2.6 Ma (Fig.3a-d). High-amplitude fluctuation in *Tsuga* content varies at glacial-interglacial time scales, implying that the temperature variation in the Heqing basin is coupled with change in the NHIS (An et al., 2011). Rb/Sr minima and TOC maxima reflect an enhanced ISM associated with interglacial ice minima, while the glacial ISM intensity can be well inferred from the TOC minima and Rb/Sr maxima (An et al., 2011). Amplitude of the ISM variability is relatively large during 1.8-0.9 Ma, compared with those in the other two time intervals. Varying amplitudes of the ISM variability through the Quaternary are attributed to different roles of the NHIS and the Antarctica temperature in driving glacial-interglacial ISM variability. During 1.8-0.9 Ma, the ISM was dominantly affected by the thermal pull of the NHIS, whereas before 1.8 Ma and after 0.9 Ma the pressure push caused by the Antarctica temperature change could offset the thermal pull effect, resulting in decreased amplitude of the glacial-interglacial ISM variability (An et al., 2011).

In the Zoige Basin, vegetation density is greatly influenced by the ISM intensity, and the AP% likely reflects temperature-induced changes in the density and elevation limit of the forest (Zhao et al., 2020). The AP% and other pollen records from the ZB reveal two major transitions of the vegetation and climate changes around 1.5 and 0.6 Ma, respectively (Fig.3e).

The latter transition is characterized by a significant shift from high-frequency oscillations of the AP% before 0.6 Ma to low-frequency fluctuations afterwards. The long-term cooling trend and two remarkable transitions reveal that the dominant factor driving vegetation change in the Zoige Basin shifted from low-latitude insolation before 1.5 Ma to high-latitude ice volume after 0.62 M. Notably, ZB AP reveals a relative cooling trend during glacials after 0.6 Ma, in contrast to the HQ tsuga content that suggests a warming trend during interglacials after 0.8 Ma. Such a discrepancy is like attributue to different sensitivities of these pollen indicators to regional changes in temperature, precipitation, and vegetation.

3.3. EAM imprints in the South China Sea sediments

$\delta^{18}O_b$ records of two ODP sites from the South China Sea share identical glacial-interglacial fluctuations over the past 2.6 Ma (Fig.4a and b, Tian et al., 2002; Clemens et al., 2008). Sawtooth-shaped variations and a gradual long-term cooling trend are evident after the MPT, suggesting globally simultaneous changes in ice volume and oceanic temperature. Extreme glaciations occurred after 0.7 Ma, corresponding to marine isotope stage (MIS) 16, followed by large-amplitude glacial-interglacial fluctuations. While planktonic foraminifera have experienced strong regional and seasonal fluctuations in temperature and freshwater balance, the saw-tooth pattern of the glacial-interglacial cycles is also evident in the post-MPT planktonic $\delta^{18}O$ record from the ODP site 1143 (Fig.4c). The Alkenone-based SST records in the South China Sea are characterized by a long-term cooling trend since ~2.6 Ma and an abrupt decrease around 0.9 Ma (Fig.4d and e, Herbert et al., 2010; Li et al., 2011). While general cooling trends are well recognized in the $\delta^{18}O_b$, $\delta^{18}O_p$, and SST records, the timing and amplitude of glacial extremes are dissimilar among these three proxies. Both $\delta^{18}O_P$ and SST variations reveal that extreme cooling first occurred during MIS 22, likely related to an abrupt increase in the Antarctic ice volume (Elderfield et al., 2012). Extreme glaciation inferred by benthic $\delta^{18}O$ occurred around 0.65 Ma, lagging the other two records by ~0.3 Myr, implying that significant expansion of the NHIS and increased ice-rafted debris in the North Atlantic likely occurred at the end of the MPT (Hodell et al., 2008; Naafs et al., 2013). Overall, these three proxies mostly reflect global climate signals, rather than the EAM imprints.

Elemental and mineral proxies from the South China Sea sediments provide valuable insights into monsoon-related changes in oceanic productivity and continental weathering (Fig.4f-h). The Ba/Al ratio of ODP site 1146, as an indicator of monsoon-driven

paleoproductivity change, displayed a long-term decreasing trend between 2.6-1.2 Ma and relatively large amplitude fluctuations afterwards (Clemens et al., 2008). In contrast, the Ti/Al ratio at ODP site 1143, as an indicator of monsoon-induced weathering intensity was enhanced remarkably around 1.6 Ma and continuously strengthened since 0.6 Ma (Tian et al., 2011), consistent with the long-term trend inferred by the mineralogical ratio of chlorite/(chlorite+hematite+goethite) (Clift et al., 2008). Unlike the generally increasing of the Ti/Al ratio, the Hm/Gt ratio from ODP Site 1143 is characterized by a gradual weakening of the summer monsoon intensity, superimposed by two stepwise shifts around 1.25 and 0.55 Ma (Zhang et al., 2007, 2009; Ao et al., 2011). Compared with the land-based proxies, these marine-based indicators exhibit different variation patterns in terms of both long-term trend and glacial-interglacial amplitude through the Quaternary, implying complicated impacts of the EAM on minearal and geochemical compositions of the South China Sea sediments (Wang et al., 2005).

3.4. Periodicities of Quaternary climate change

To assess the evolution of climatic periodicity during the Quaternary, wavelet and power spectral analyses were performed on representative proxy records using the Acycle software of Li et al. (2019). Wavelet and power spectra of six representative proxies from loess and lake archives are presented to address periodic evolution of the EAM and ISM changes on land (Fig.5). Mean grain-size stack (MGS) from XF/LT loess sections is characterized by an onset of a weak 100-kyr cycle at ~1.2 Ma, followed by strong 100-kyr cycles after ~0.7 Ma (Sun et al., 2006a). Obliquity cycle is relatively stronger before 0.7 Ma than afterwards due to the growing influence of the 100-kyr ice-age cycles, while the precession cycles are very weak and discontinuously present through the Quaternary (Fig.5a). Similar periodic transition during the MPT was also found in other grain-size (Liu et al., 1999; Ding et al., 2002) and MS time series (Heslop et al., 2002; Lu et al., 2004). Over the past 2.6 Ma, relative intensities of spectral peaks at three orbital periods slightly differ between MGS and MS time series. Besides the strong 41-kyr cycles, the MGS spectrum displays relatively weak 100-kyr cycle and distinct 23- and 19-kyr peaks, differing from the persistent strong 100-kyr peak and insignificant precession cycle in the MS spectrum. Unlike loess proxies from the central CLP, the wavelet spectrum of JY $\delta^{13}C_{IC}$ record shows a different transition from a dominant 23-kyr cycle prior to 1.2 Ma, to combined 100- and 41-kyr cycles afterwards (Sun et al., 2019).

For two lake records, wavelet and power spectra of three proxies exhibit different

characteristics at three orbital periods (Fig.5d-f). The spectrum of the HQ ISM index exhibits a combined pattern of three orbital periods before 1.8 Ma and after 0.9 Ma, and a dominant 41-kyr cycle between 1.8-0.9 Ma (An et al., 2011). Besides three orbital periods in the ISM index, the spectum of HQ Tsuga content reveals more orbital harmonic periodicities. This evolution pattern is consistent with different roles of the NHIS and the Antarctica temperature in driving the ISM variability. Unlike the complex spectra of HQ proxies, the AP% spectrum exhibits a persistent 41-kyr cycle through the last 1.7 Myr, as well as a strong 19-kyr cycle until 0.6 Ma and a clear 100-kyr cycle after 0.6 Ma (Fig.5f). The spectral results of these loess- and lake-derived proxies confirm diverse expression of Quaternary monsoon changes on the land.

Wavelet and power spectra of five proxy indicators from ODP site 1143 and the Ba/Al ratio of ODP site 1146 also exhibit different evolving periodicities of monsoon-related changes in the South China Sea (Fig.6). Similar to the global benthic $\delta^{18}O$ stack (Lisiecki and Raymo, 2005), $\delta^{18}O_b$ spectrum shows an evident MPT from 41-kyr to 100-kyr cycles around 1.2 Ma, consistent with the spectra of SST and Ba/Al records. In contrast, $\delta^{18}O_p$ spectrum exhibits a mixed pattern of 100-, 41-, 23/19-kyr periods before 1.8 Ma, quite similar to those of the Ti/Al and Hm/Gt ratios. Since 1.8 Ma, the $\delta^{18}O_p$ spectrum also displays a transition from 41 to 100 kyr cycles around 1.2 Ma, whereas both 41- and 100-kyr cycles are persistently present in the other two proxies. Notably, evolutionary spectra of the Ti/Al and Hm/Gt ratios show all orbital peaks at 100, 41, 23, and 19-kyr bands, and no clear transition in periodicity is found across the MPT. Since the 23- and 19-kyr cycles are discontinuously presented in the spectra of the Ti/Al and Hm/Gt ratios, implying a distinct impact of insolation on the chemical weathering in the source areas of the South China Sea sediments. Moreover, presence of the 100-kyr cycles in most of the marine-based proxies, particularly during the early Pleistocene, confirms that eccentricity likely plays a key role in modulating low-latitude oceanic changes (Clemens et al., 1997).

Based on the relative weights of three orbital peaks in the spectral results (Figs.5 and 6), we further characterize these terrestrial and marine proxy records into four types. Type 1 (loess MGS and MS, $\delta^{18}O_b$, SST, and Ba/Al ratio) is characterized by the conventional transition from 41- to 100-kyr cycles between 1.2-0.7 Ma, which are strongly coupled with the NHIS change Type 2 (ZB AP%, HQ ISM and Tsuga content, and ODP1143 $\delta^{18}O_p$) displays a shift from mixed 41- and 23-kyr cyclicities to a combination of 100-, 41- and 23-

kyr cycles, implying that combined effects of astronomical and ice/CO_2 forcing were persistent during the Quaternary. Type 3 (JY $\delta^{13}C_{IC}$) exhibits a shift from 23-kyr to mixed 100-, 41- and 23-kyr cycles, indicating a shift from the dominant insolation forcing to combined insolation and ice/CO_2 forcing across the MPT. Type 4 (Ti/Al and Hm/Gt ratios of ODP1143 sediments) exhibits persisitent 100-, 41-, and 23-kyr cycles without significant periodicity shift through the Quaternary implying complicated roles of glacial and/or eccentricity forcing in driving Quaternary climate change.

We found that proxy records (Type 1) associated with changes in annual temperature and winter wind usually display a traditional MPT from 41-kyr to 100-kyr cycles during 1.2-0.7 Ma. However, proxy records related toies reflecting monsoon-induced precipitation and weathering processes (Types 2-4) exhibit a diverse manifestation of the MPT from mid-latitude lake and loess sediments to low-latitude marine sediments. For example, the JY $\delta^{13}C_{IC}$ and ZB AP% are highly sensitive to vegetation changes in the monsoon-affected region (Sun et al., 2019; Zhao et al., 2020), displaying strong precession cycles through the Quaternary. In the low-latitude ocean, chemical weathering indicators (e.g. Hm/Gt and Ti/Al ratios) are sensitive to monsoon-induced weathering intensity over the southern China (Zhang et al., 2007; Ao et al., 2011; Tian et al., 2011), demonstrating a persistent 100-kyr periodicity during the Quaternary. In addition, persistent 400-ka cyclicity has been inferred from carbon isotope of the South China Sea sediments (Wang et al., 2003) and magnetic parameter of the Tengger Desert sediments (Liu et al., 2021). Continued obliquity pacing was identified in the Sr/Ca ratio of microcodium in loess deposit (Li et al., 2017), whilst dominant precession cycles were identified in the Chinese speleothem $\delta^{18}O$ records (Wang et al. 2008; Cheng et al., 2016). We group these three proxy records as a unique type (Type 5), as only one periodicity was persistently dominated through the Quaternary. Regardless of the type, mechanisms underlying these diverse manifestations still need further assessments by direct proxy-model comparison.

4. Dynamics of orbital-scale monsoon change in East Asia

4.1 Outstanding issues of orbital-scale monsoon dynamics

Orbital-scale climate changes in the Asian monsoon-affected region are primarily controlled by orbital-induced changes in solar insolation, ice volume, atmospheric concentrations of greenhouse gases, interhemispheric thermal and pressure gradients (e.g. An

et al., 1991a, 2011, 2015; Ding et al., 1995; Wang et al., 2017; Cheng et al., 2021; Clemens et al., 2021). The periodic variations of three astronomical parameters (eccentricity, obliquity, and precession) lead to seasonal changes in incoming solar radiation received at Earth's surface (Berger, 1978), resulting in different land-sea thermal and pressure contrasts that affect the monsoon variability (Kutzbach and Guetter, 1986; Prell and Kutzbach, 1987). Meanwhile, the NHIS can affect the strength of monsoon circulations mainly through meridional temperature gradient between high- and mid-latitude regions (An et al., 2001; Wen et al., 2016; Shi et al., 2021), as well as atmospheric teleconnection induced by ice sheet topography (Yin et al., 2008, 2009). Concentrations of greenhouse gases (particularly CO_2) also influence monsoon variability by affecting temperature gradient between high- and low-latitude regions and migration of the intertropical convergence zone (ITCZ) (Felzer et al. 1998; Lu et al., 2013). Impacts of these forcing factors on monsoon variability have been separately evaluated by proxy records (e.g. Guo et al., 2012; Sun et al., 2015) and model results (Yin et al., 2008, 2009; Wen et al., 2016). However, direct comparisons of proxy records with model results (e.g. TRACE21, HadCM3) have provided further assessments of orbital-scale climate dynamics (e.g., Liu et al., 2014; Sun et al., 2019; Cheng et al., 2021).

The monsoon was originally defined as the seasonal reversal in prevailing wind direction between land and sea and subsequently linked to seasonal precipitation variation (e.g. Dash, 2005; Wang, 2006, and references therein). In modern meteorological observations, there are many definitions of the monsoon index (e.g. Wang et al., 2008), among which the most commonly accepted one is the seasonal variation of precipitation (Wang and Ding, 2008; Geen et al., 2020). In geological records, loess grain-size is the most direct indicator of winter monsoon intensity (An et al., 1991b; Xiao et al., 1992). By contrast, the intensity of summer monsoon is mostly inferred from indirect indicators, such as the pedogenic intensity (An et al., 1991a), geochemical and mineralogical ratios (Guo et al., 1996; Chen et al., 1999), vegetation density (An et al., 2005; Yang et al., 2015), and oxygen isotope compositions of monsoonal precipitation (Wang et al., 2001). However, these summer monsoon-related indicators are usually affected by other factors such as temperature and water vapor sources, and thus exhibit relatively complex characteristics of orbital-scale variability (e.g. Clemens et al., 2010; Cai et al., 2015; An et al., 2015; Cheng et al., 2021).

Recently, orbital-scale changes in paleo-precipitation and temperature have been quantitatively reconstructed using biomarkers and ^{10}Be in Chinese loess (Peterse et al., 2014;

Thomas et al., 2016; Beck et al., 2018; Lu et al., 2019). Seawater oxygen isotopic composition after quantitatively removing of temperature impact has been utilized to infer the river runoff change related to regional monsoon precipitation (Gebregiorgis et al., 2018; Clemens et al., 2018, 2021). These quantitative indicators are helpful for in-depth deciphering different effects of temperature and precipitaton on monsoonal proxy records. To help disentangle this complexity, model simulations can also be directly employed to assess the responses of different climatic variables such as temperature, precipitation and wind intensity to the individual and combined effects of astronomical, ice, and CO_2 forcing (Yin et al., 2009; Lu et al., 2013; Liu et al., 2014; Wen et al., 2016; Lyu et al., 2021). Direct comparison of these model results with proxy variability over the East Asian monsoon-affected region will facilitate the dynamical understanding of orbital-scale monsoon change during the Quaternary.

4.2 Pre-industrial seasonal changes in temperature, precipitation, and southerly wind

The relative sensitivity of the ISM and EAM to changes in orbital parameters, ice volume, and CO_2 have been addressed quantitatively using an emulator approach based on 61 sensitivity experiments performed by the HadCM3 model (Araya–Melo et al., 2015; Sun et al., 2019; Lyu et al., 2021). The assessment of multi-model simulation on East Asia suggests that HadCM3 can well the annual and seasonal surface air temperature and precipitation climatology in East Asia (Jiang et al., 2005). The HadCM3 model has been shown to capture well enough the monsoon–ENSO interaction and natural variability of the summer rainfall over China (Li et al., 2007; Lei et al., 2014). In these experiments, three astronomical parameters (eccentricity, longitude of perigee, and obliquity), CO_2 concentrations (180-280 ppmv), and glaciation levels of ice extent and height ranging from Holocene to Last Glacial Maximum are included to represent different astromonical, ice sheets, and CO2 configurations (for a detail experiment design, see Tabhle 1 in Araya–Melo et al., 2015). Here we employ the same emulator approach to quantitatively address different sensitivities of temperature, precipitation, southerly wind (V-wind) changes to orbital parameters, CO_2, and ice volume forcing. The simulated changes in summer temperature (T-Summer), summer precipitation (P-summer), near-surface summer southerly wind (V-summer), annual temperature (T-annual), and annual precipitation (P-annual) are the estimated equilibrium responses of the HadCM3 for forcing conditions spanning the Quaternary by steps of 1 kyr. The simulated results under different orbital, ice and CO_2 configurations were averaged over six latitudinal zones (i.e. 0-10° N, 10-20° N, 20-30° N, 30-40° N, 40-50° N, and 50-60° N)

between 105-120° E, where climate changes are sensitive to both ISM and EAM variability.

Based on the model results, we first present seasonal changes in precipitation, temperature and southerly wind over the six latitudinal zones under the pre-industrial condition (Fig.7). Precipitation changes in five zones all show distinct seasonal cycles with high in summer and low in winter, except for the low-latitude ocean (0-10ºN). From south to north, seasonal contrasts of precipitation at 10-30ºN are significantly greater than those at 30-60ºN. The rainy season is relatively long lasting from April to September at 10-30ºN, compared to those concentrated in June to August at 30-60ºN. The seasonal characteristic of temperature variation is opposite to that of precipitation change, displaying gradually increasing amplitudes from low latitudes to high latitudes. In the two low-latitude zones of 0-20ºN, the seasonal contrast of temperature is less than 5ºC. From 20ºN north, the seasonal variation of temperature gradually increases from 15 to 50ºC. Such a spatial pattern in seasonal temperature changes is mainly related to winter temperature difference, because the difference in summer temperature is less than 10ºC over the six latitudinal zones (Fig.7b).

The southerly wind intensity in summer season can be regarded as a direct indicator of the summer monsoon strength (Liu et al., 2014). Seasonal variations of southerly wind intensity over six latitudinal zones suggest that the summer monsoon influence is more significant at 0-40ºN than at 40-60ºN (Fig.7c), consistent with the northern limit of summer monsoon front is around 40-45ºN (Ding and Chan, 2005). Seasonal variations of southerly wind intensity in low-latitude region (0-10ºN) are significantly higher than that in mid-latitude regions (30-40ºN). In the area north of 40ºN, the seasonal variation of southerly wind is not obvious, while the easterly wind shows obvious seasonal reversal. Seasonal changes in precipitation and southerly winds intensity are coupled in the low-latitude (10-20ºN) ocean and mid-latitude (20-40ºN) land, implying that middle-to-low latitudes of East Asia (10-40ºN) are sensitive to changes in both monsoonal wind and precipitation. Unlike the dominant ISM and EAM influences in the summer season, East Asia in the winter season is jointly affected by the winter monsoon and westerly circulation, characterized by less precipitation and lower temperature. Therefore, the characteristics and controlling factors of climatic elements in winter will not be detailed in the following section.

4.3 Impacts of different forcing on temperature, precipitation and wind changes

The remarkable feature of the monsoon climate in East Asia is the strong coupling between heavy rainfall and high temperature in the summer season. However, it is often

difficult to distinguish the effects of summer or annual temperature and precipitation on these proxy indicators. Therefore, five climate variables (i.e. T-summer, P-summer, V-summer, T-annual, and P-annual) will be further analyzed to quantify different effects of astronmical parameters, CO_2 and ice volume. The response sensitivities of these five variables were calculated over six latitudinal zones during two time intervals of 2-1.2 Ma and 0.8-0 Ma. The major differences of these forcing factors across the MPT are the ice extent and CO_2 concentration during glacial maxima (Lisiecki and Raymo, 2005; Hönisch et al., 2009; Araya-Melo et al., 2015). Thus sensitivity analyses were based on full glacial-interglacial ranges of the ice levels (1-11) and CO_2 concentrations (180-280 ppmv) after the MPT and half ranges of the ice levels (1-6) and CO_2 concentrations (220-280 ppmv) before the MPT.

The sensitivity results show that the precession, obliquity, CO_2, and ice play different roles in affecting these climate variables (Fig.8). After the MPT (Post-MPT, Figs. 8a-c**),** precession is the dominant factor affecting three summer climate variables, while obliquity only plays limited influence on T-summer and P-summer at 30-60ºN. Compared to two astronomical parameters, CO_2 has a weak effect on S-Temp, but hardly affects P-summer and V-summer changes. Ice volume has a relatively small effect on S-Temp, and its impact on V-summer wind is mainly manifested at 0-10ºN and 40-60ºN. Moreover, ice volume significantly affects the P-summer change at 0-30ºN. Before the MPT (Prior-MPT, Figs. 8f-h), the precession played a more dominant role in affecting the summer climate variablies than the other three forcing factors. The relative effects of both CO_2 and ice sheets were strongly weakened, due to increased CO_2 concentration and decreased ice extent during the moderate glaciations before the MPT.

For the T-annual and P-annual changes, relative roles of these four forcing are quite different from those for the summer variables. After the MPT, the T-annual change is mainly affected by CO_2 and precession, and the impact of CO_2 is greater than the precession (Fig.8d). Ice volume only affects the T-annual over northern regions (30-60ºN). The P-annual change (Fig.8e), however, is mainly affected by precession and ice volume, and less influenced by obliquity and CO_2. In the southern region (0-30ºN), the P-annual is mainly affected by ice volume change, whereas in the northern region (30-60ºN), the P-annual is jointly affected by precession, obliquity, CO_2, and ice forcing, with precession being the dominant driving factor. Before the MPT, the impact of precession on T-annual is greater than those of CO_2 and ice (Fig.8i). The precession's effect on P-annual is more evident than the ice in the northern

region (30-60 ºN), but its influence becomes relative weaker than ice in the southern region (0-30ºN) (Fig.8j). In summary, precession plays a dominant role in affecting summer climate variables, whears ice and CO_2 play quite different roles in affecting the P-annual and T-annual, respectively.

5. Diverse regional sensitivitity to astromonical, ice, and CO_2 forcing

5.1 Spatial differences in response to astronomical, ice, and CO_2 forcing

Meteorological observation data reveal that the spatial pattern of the inter-decadal variability of summer precipitation in China is mainly structured with two meridional modes: the dipole (southern vs. northern China) pattern and the positive-negative-positive ((southern China-Yangtz River valley-northern China) pattern (Ding et al., 2008). Proxy records and model results also reveal similar spatial patterns of precipitation (i.e. Liu et al., 2014; Zhang et al., 2018). Our modeling results reveal that the impacts of four driving factors on temperature and precipitation changes are also spatially different after the MPT. The influence of precession on T-summer is most significant in mid-latitude regions (20-40ºN) (Fig.8a), and its influence on T-annual gradually increases from low- to mid-latitude regions (Fig.8d). The influence of precession on summer and annual precipitation is significantly stronger in three northern zones (30-60ºN) than in the southern zones (0-30ºN) (Fig.8c and e). Obliquity slightly affects T-summer, P-summer, and P-annual in the northern zones. CO_2 has distinct effects on T-summer in the southern zones and P-annual in the northern zones. Ice volume has a greater impact on P-summer and P-annual in the south than in the north, since the ice sheet plays an important role in the migration of the Intertropical Convergence Zone (Lyu et al., 2021). Meanwhile, ice impact on T-annual is greater in the northern zones than in the southern part.

The spatial differences of the sensitivity results in response to these four forcing factors are slightly different before and after the MPT. Before the MPT, the influence of precession on S-Temp is spatially consistent, whereas its influences on summer and annual precipitations are stronger in the northern zones than in the southern zones. The influence of ice volume on summer and annual precipitation is stronger in three southern zones than in the northern zones. Due to the relatively low ice extent and high CO_2 concentration during glacial times before the MPT, the influences of CO_2 on temperature and ice on precipitation are significantly weakened. Clearly, the sensitivities of temperature and precipitation responses to astronomical,

ice and CO_2 forcing are spatially different between north and south at 30ºN. Such a north-south difference is particularly evident for the precipitation response. Therefore, we will consider the regional response differences to further discuss orbital-scale climate variability and mechanisms in the follow section.

5.2. Comparison between simulated results in north and south China

Simulated changes of five climate variables spanning the last 2.6 Ma are compared between two sensitive regions (South China, 20-30ºN; North China, 30-40ºN) (Fig.9). T-summer in South China is generally higher than that in North China, but its varying magnitude is smaller than that in North China. T-summer changes in the two regions are predominantly controlled by the precession-induced summer insolation. The V-summer changes in the two regions are also dominated by precession cycles, while the intensity and variability of V-summer in South China are significantly higher than those in North China. By contrast, the P-summer changes in the two regions are quite different. The P-summer in South China is relatively high and exhibits significant variability at both glacial-interglacial and precession time scales,whereas the P-summer in North China is less variable but dominated by precession cycles. Changes of P-summer and V-summer in North China are quite highly correlated, whereas variations of these two variables are decoupled in South China. Changes in T-annual and P-annual are generally similar in the two regions. The amplitude and variability of these two variables in South China are larger than those in North China. The T-annual and P-annual vary from 8.5-11.5ºC and 21-28 mm in North China to 17-20ºC and 45-60 mm in South China, respectively.

Wavelet Spectra of these simulated climate variables are presented to further decipher regional differences in the evolving orbital periodicities (Fig.10). Spectra of the T-summer and V-summer in these two regions are dominated by consistently strong precession cycles. P-summer in North China is also dominated by persistent precession cycles, but exhibits a mixing pattern of 100, 41, 23 and 19-kyr periodicities in South China. The T-annual spectra are similar between these two regions, characterized by strong precession and weak obliquity cycles over the last 2.6 Ma and a significant 100-kyr cycle after 0.7 Ma (Type 2). The P-annual spectra, however, are apparently different between North and South China. The A-Prec in North China is dominated by persistent precession cycles over the last 2.6 Ma and a strong 100-kyr cycle since 0.7 Ma (Type 3), implying a strong influence of ice volume after the MPT. In South China, P-annual spectrum shows a strong 41-kyr cycle between 2.6-0.7 Ma and a

dominant 100-kyr period after 0.7 Ma, implying that the ice volume played a significant impact on the annual precipitation.

The simulation results show that different climate variables can indeed exhibit diverse manifestations of orbital-scale changes through the Quaternary. Similar to the five types of orbital-scale variability inferred from proxies records, the simulated climate variables over two regions can be grouped into four types. P-annual in South China share similar evolving spectrum as the Type 1 (Fig.10j). Wavelet spectra of P-summr and T-annual in South China are identical to that of Type 2, characterized by a shift from 41/23-kyr to 100/41/23-kyr cylces (Fig.10h and i). P-annual in North China displays a period shift from persistent 23-kyr through the Quaternary to 100/23-kyr cycles after 0.7 Ma (Type 3, Fig.10e). The other five variables (T-summer and V-summer in both regions, and P-summer in North China) corresponding to Type 5 dominanted by persistent precession cycles. It's noteworthy that model results don't exhibit persistent 400-, 100-, or 41-kyr cycles throughout the Quaternary.

5.3 Implications of proxy-model comparison

To assess the sensitivity of different proxies to climate variables, proxy indicators from lake, loess and stalagmite records are directly compared with simulated temperature and precipitation changes. Comparison of three proxies from Heqing paleolake with simulation results at 20-30ºN suggested that *Tsuga* content, TOC content, and ISM index likely respond well to changes in annual temperature, summer precipitation, and annual precipitation, respectively (Fig.11a-c). The *Tsuga* content mainly reflects the annual temperature range, which is strongly associated with the winter temperature change (An et al., 2011). Therefore, the *Tsuga* content exhibits similar variability to the simulated T-annual change, in terms of both amplitude and rhythms. The TOC content in the Heqing paleolake is sensitive to monsoon-induced biomass change in the lake catchment particularly during the interglacial periods, and thus matches well with the simulated P-summer change. By contrast, ISM index can capture both glacial weakening and interglacial strengthening of the monsoon intensity, and thus corresponds well to the P-annual change. Wavelet coherence spectra suggest that these three proxy records are strongly coupled with changes in T-annual, P-summer and P-annual, respectively (Fig.11d-f). Strong coherency at 100-kyr period after the MPT confirms the significant ice effects on the P-summer and P-annual, and ice/CO_2 effects on T-annual in South China. The coherency at precession band is evident in the Tsuga/T-annual and TOC/P-summer spectra, but unclear in the ISM/P-annual spectrum, consistent with different impacts

of insolation on temperuate and precitation changes in the same region..

Since the age models for loess, lakes, and stalagmite records are established by different approaches, the chronological uncertainties make it difficult to perform a cycle-by-cycle correlation between the proxies and model results. Nevertheless, good match between these proxy records with the simulation results at 30-40ºN suggests that ZB AP concentration, cave $\delta^{18}O$ and loess $\delta^{13}C_{IC}$ are sensitive to changes in T-annual, P-summer, and P-annual, respectively (Fig.12a-c). The AP content in the ZB sediments shows significant glacial-interglacial variability after 0.6 Ma, consistent with the simulated T-annual change. However, marked decrease in the AP content after 0.6 Ma than before, especially during the glacial times, is not evident in the simulated T-annual change. Variation of the composite $\delta^{18}O$ records from Hulu/Sanbao caves is quite similar to the simulated P-smmer change, characterized by dominant precession cycles. The loess $\delta^{13}C_{IC}$ variability is very similar to the simulated P-annual change, showing distinctive shifts from dominant precession cycles to combined glacial-interglacial and precessional fluctuations accross the MPT. Coherency spectra between these three proxies and simulated results reveal that precssion and ice/CO2 forcing jointly affect orbital-sclae changes in annual temperature and precipitation changes in North China, whereas summer precipitation is predominantly driven by precession-induced insolation change (Fig.12e-f).

The diverse nature of proxy fluctuations and model results during the Quaternary can be attributed to two major reasons: (1) different sensitivities of proxy indicators to precipitation and temperature changes, and (2) different responses of temperature and precipitation changes to external (insolation) and internal (ice volume) forcing. Formation of Chinese loess-paleosol sequences is not only related to ice volume-induced changes in source aridity and winter monsoon intensity (An et al., 1991a; Ding et al., 1995), but also influenced by precipitation-induced changes in pedogenesis and chemical weathering (An et al., 1991b; An, 2000). Therefore, Chinese loess can simultaneously document both 100-kyr cycles of the source aridity and winter monsoon intensity coupled with the NHIS change and 21-kyr signal of hydroclimate change associated with insolation-driven changes in land-ocean thermal and pressure gradients. Stalagmites, however, are greatly influenced by the hydroclimate change, thus its $\delta^{18}O$ values likely reflect combined changes in precipitation, large-scale changes in monsoon ciuculatoin and moisture sources (Wang et al., 2001, 2008; Clemens et al., 2010; Clemens et al., 2018; Cai et al., 2015; Cheng et al., 2016, 2021). In north China, simulated

changes in summer precipitation and southerly wind are strongly coupled. Therefore, different cyclicities between JY $\delta^{13}C_{IC}$ and speleothem $\delta^{18}O$ is related to the intrinsic characteristics of the two proxy records (i.e. summer vs. annual precipiation), rather than controversial orbital-scale monsoon dynamics.

6. Conclusions and prospects

Representative proxy records from loess, stalagmites, lake, and marine sediments have been synthesized to address the spatiotemporal patterns of Quaternary climate change in East Asia. Changes in loess grain size, sea surface temperature, benthic and planktonic oxygen isotopes in south China Sea seiments show strongly 100-kyr cycles after the MPT, since they are sensitive to ice volume and/or CO2 forcing. However, several hydroclimatic and weathering proxies (e.g. loess $\delta^{13}C_{IC}$, lake proxies, and mineral/chemical compositions in South China Sea sediments) are characterized by strong 23-kyr cycles or mixed 41-kyr and 23-kyr cycles, together with distinct 100-kyr cycles after the MPT. The coexistence of 100-, 41i, and 23-kyr cycles illustrates the combined effects of astronomical, ice, and CO_2 forcing on Quaternary climate change in East Asia. Modeling results suggest that responses of temperature and precipitation to insolation, ice, and CO_2 forcing are spatially different. In North China (30-40ºN), insolation plays a predominant role in driving temperature and precipitation changes during the summer season, while ice and CO_2 play more dominant roles in affecting the annual precipitation and temperature changes, respectively. In South China (20-30ºN), responses of different climate variables to four forcing factors are also dissimilar. Insolation mainly affects the summer temperature change, while the annual temperature change is influenced by both insolation and CO_2, and the summer and annual precipitation changes are strongly influenced by glacial forcing.

Our proxy-model comparison suggests that the Quaternary climate changes in East are jointly driven by insolation, ice, and CO_2 changes, while their effects on different climate elements are quite different on both seasonal and regional scales. Our synthesis suggests that diverse expressions of evolving periodicities in the proxies are attributable to their different reponses to precipitation and temperature changes. Meanwhile, different sensitivities of temperature and precipitation to external and internal forcing should be involved when addressing the dynamics of orbital-scale climate change inferred from different proxies from various archives. To better decipher orbital-scale monsoon changes and dynamics, high-

resolution and quantitative reconstruction of paleotemperature and paleoprecipitation changes are crucial for robust proxy-model comparison. The potential effect of provenance shifts on mineral and geochemical proxies should also be considered when addressing Quaternary climate change using physiochemical indicators. Meanwhile, transient simulations that incorporate both external forcing and internal feedbacks using high-resolution regional Earth climate system models shoul be performed to generate more reliable climate variables for model-proxy comparison. Moreover, multi-scale interactions, e.g. the cumulative effect of the North Atlantic abrupt events and the modulation effect of asynchronous development of bi-polar ice-sheets on orbital-scale climate changes, should be assessed using more sensitivity experiments. Lastly direct comparison of quantitatively reconstructed temperature and precipitation data with climate variables output from high-resolution regional Eath Climate System models is the most efficent approach for future assessments of orbital-scale climate change and dynamics in a global context.

Authors' contributions: Youbin Sun, Steven Clemens, and Zhisheng An initiated this work. Ting Wang, Yanjun Cai, and Li Ai collected the proxy records. Qiuzhen Yin, Anqi Lyu, and Michel Crucifix analyzed the modeling results. All authors contributed to data interpretation and preparation of manuscript.

Acknowledgements:

This work was supported by grant from the Chinese Academy of Sciences (No. XDB40000000). MC is Research Director and QZY is Research Associate of the Belgian National Fund of Scientific Research. A. Lyu is supported by the grants from the UCLouvain and China Scholarship Council (CSC) Grant #201706190226. Computational resources have been provided by the supercomputing facilities of the Université catholique de Louvain (CISM/UCL) and the Consortium des Équipements de Calcul Intensif en Fédération Wallonie Bruxelles (CÉCI) funded by the Fond de la Recherche Scientifique de Belgique (F.R.S.-FNRS) under convention 2.5020.11.

References:

An, Z., 2000. The history and variability of the East Asian paleomonsoon climate. Quat. Sci. Rev. 19, 171–187.

An, Z., Clemens, S.C., Shen, J., Qiang, X., Jin, Z., Sun, Y., Prell, W.L., Luo, J., Wang, S., Xu, H., Cai, Y., Zhou, W., Liu, X., Liu, W., Shi, Z., Yan, L., Xiao, X., Chang, H., Wu, F., Ai, L., Lu, F., 2011. Glacial–interglacial Indian summer monsoon dynamics. Science 333, 719–723.

An, Z.S., Colman, S.M., Zhou, W.J., Li, X.Q., Brown, E.T., Jull, A.J.T., Cai, Y.J., Huang, Y.S., Lu, X.F., Chang, H., Song, Y.G., Sun, Y.B., Xu, H., Liu, W.G., Jin, Z.D., Liu, X.D., Cheng, P., Liu, Y., Ai, L., Li, X.Z., Liu, X.J., Yan, L.B., Shi, Z.G., Wang, X.L., Wu, F., Qiang, X.K., Dong, J.B., Lu, F.Y., Xu, X.W., 2012. Interplay between the Westerlies and Asian monsoon recorded in Lake Qinghai sediments since 32 ka. Sci. Rep., 2, 619.

An, Z., Huang Y., Liu, W., Guo, Z., Clemens, S.C., Li, L., Prell, W., Ning, Y., Cai, Y., Zhou, W., Lin,B., Zhang, Q., Cao, Y., Qiang, X., Chang, H., Wu, Z., 2005. Multiple expansions of C4 plant biomass in East Asia since 7 Ma coupled with strengthened monsoon circulation. Geology 33, 705–708. https://doi.org/10.1130/G21423.1.

An, Z., Kukla, G.J., Porter, S.C., Xiao, J., 1991a. Late quaternary dust flow on the Chinese Loess Plateau. Catena 18, 125–132.

An, Z., Kukla, G.J., Porter, S.C., Xiao, J., 1991b. Magnetic susceptibility evidence of monsoon variation on the Loess Plateau of central China during the last 130,000 years. Quat. Res. 36, 29–36.

An, Z., Kutzbach, J.E., Prell, W.L., Porter, S.C., 2001. Evolution of Asian monsoon and phased uplift of the Himalaya-Tibetan plateau since late Miocene times. Nature, 411.

An, Z., Liu, T., Lu, Y., Porter, S.C., Kukla, G.J., Wu, X., Hua, Y., 1990. The long–term paleomonsoon variation recorded by the loess–paleosol sequence in central China. Quat. Int. 7/8, 91–95.

An, Z., Wu, G., Li, J., Sun, Y., Liu, Y., Zhou, W., Cai, Y., Duan, A., Li, L., Mao, J., Cheng, H., Shi, Z., Tan, L., Yan, H., Ao, H., Chang, H., and Feng, J., 2015. Global monsoon dynamics and climate change. Annu. Rev. Earth Planet. Sci. 43, 29–77. https://doi.org/10.1146/annurev-earth-060313-054623.

Ao, H., Dekkers, M.J., Qin, L., Xiao, G., 2011. An updated astronomical timescale for the Plio–Pleistocene deposits from South China Sea and new insights into Asian monsoon evolution. Quat. Sci. Rev. 30, 1560–1575.

Ao, H., Rohlinge, E.J., Stringer, C., Roberts, A.P., Dekkers, M.J., Dupont-Nivet, G., Yu, J., Liu, Q., Zhang, P., Liu, Z., Ma, X., Zhou, W., Jin, Z., Xiao, G., Wang, H., Sun, Q., Yang, P.G., Peng, X., Shi, Z., Qiang, X., An, Z., 2020. Two-stage mid-Brunhes climate transition and mid-Pleistocene human diversification. Earth Sci. Rev. 210, 103354.

Araya–Melo, P.A., Crucifix, M., Bounceur, N., 2015. Global sensitivity analysis of the Indian monsoon during the Pleistocene. Clim. Past 11, 45–61.

Beck, J.W., Zhou, W., Li, C., Wu, Z.K., White, L.,Xian, F., Kong, X.H., An, Z.S., 2018. A 550,000-year record of East Asian monsoon rainfall from ^{10}Be in loess. Science, 360, 877–881.

Bemis, B.E., Spero, H.J., Bijma, J., Lea, D.W., 1998. Reevaluation of the oxygen isotopic composition of planktonic foraminifera, Experimental results and revised paleotemperature equations. Paleoceanography 13, 150–160.

Berger, A., 1978. Long-term variations of daily insolation and Quaternary climatic changes. J. Atmos. Sci. 35, 2362–2367.

Berger, A., Crucifix, M., Hodell, D.A., Mangili, C., McManus, J.F., Otto-Bliesner, B., Pol, K., Raynaud, D., Skinner, L.C., Tzedakis, P.C., Wolff, E.W., Yin, Q., Abe-Ouchi, A., Barbante, C., Brovkin, V., Cacho, I., Capron, E., Ferretti, P., Ganopolski, A., Grimalt, J.O., Hönisch, B., Kawamura, K., Landais, A., Margari, V., Martrat, B., Masson-Delmotte, V., Mokeddem, Z., Parrenin, F., Prokopenko, A.A., Rashid, H., Schulz, M., Riveiros, N.V., 2016. Interglacials of the last 800,000 years. Rev. Geophys. 54, 162–219. https://doi.org/10.1002/2015RG000482.

Berger, A., Imbrie, J., Hays, J., Kukla, G., Saltzman, B., 1984. Milankovitch and Climate. Springer, Dordrecht. https://doi.org/10.1007/978-94-017-4841-4.

Betzler, C., Eberli, G.P., Lüdmann, T., Reolid, J., Kroon, D., Reijmer, J.J.G., Swart, P.K., Wright, J., Young, J.R., Alvarez-Zarikian, C., Alonso-García, M., Bialik, O.M., Blättler, C.L., Guo, J.A., Haffen, S., Horozal, S., Inoue, M., Jovane, L., Lanci, L., Laya, J.C., Hui Mee, A.L., Nakakuni, M., Nath, B.N., Niino, K., Petruny, L.M., Pratiwi, S.D., Slagle, A.L., Sloss, C.R., Su, X., and Yao, Z., 2018. Refinement of Miocene sea level and monsoon events from the sedimentary archive of the Maldives (Indian Ocean). Prog. Earth Planet. Sc. 5(1), 5. https://doi.org/10.1186/s40645-018-0165-x.

Bloemendal, J., Liu, X., Sun, Y., Li N., 2018. An assessment of magnetic and geochemical indicators of weathering and pedogenesis at two contrasting sites on the Chinese Loess plateau. Palaeogeogr., Palaeoclimatol., Palaeoecol. 257, 152–168.

Boulay, S., Colin, C., Trentesaux, A., Frank, N., Liu, Z., 2005. Sediment sources and east asian monsoon intensity over the last 450 ky. mineralogical and geochemical investigations on south china sea sediments. Palaeogeogr. Palaeoclimatol. Palaeoecol. 228(3-4), 260–277.

Cai, M., Fang, X., Wu, F., Miao, Y., Appel, E., 2012. Pliocene-Pleistocene stepwise drying of Central Asia: Evidence from paleomagnetism and sporopollen record of the deep borehole SG-3 in the western Qaidam Basin, NE Tibetan Plateau. Glob. Plant. Change 94-95, 72–81.

Cai, Y., Fung, I.Y., Edwards, R.L., An, Z., Cheng, H., Lee, J.-E., Tan, L., Shen, C., Wang, X., Day, J.A., Zhou, W., Kelly, M.J., Chiang, C.H., 2015. Variability of stalagmite-inferred Indian monsoon precipitation over the past 252,000 y. Proc. Natl. Acad. Sci. USA 112, 2954–2959. https://doi.org/10.1073/pnas.1424035112.

Caley, T., Malaize, B., Revel, M., Ducassou, E., Wainer, K., Ibrahimd, M., Shoeaibd, D., Migeonc, S., Marieua, V., 2011. Orbital timing of the Indian, East Asian and African boreal monsoons and the concept of a "global monsoon". Quat. Sci. Rev. 30, 3705–3715. https://doi.org/10.1016/j.quascirev.2011.09.015.

Chang, H., An, Z., Liu, W., Qiang, X., Song, Y., Ao, H., 2012. Magnetostratigraphic and paleoenvironmental records for a Late Cenozoic sedimentary sequence drilled from Lop Nor in the eastern Tarim Basin. Glob. Planet. Change 80–81, 113–122.

Chen, F., Li, J., Zhang, W., 1991. Loess stratigraphy of the Lanzhou profile and its comparison with deep-sea sediment and ice core record. Geojournal 24(2), 201–209.

Chen, F.H., Chen, J.H., Huang, W., Chen, S.Q., Huang, X.Z., Jin, L.Y., Jia, J., Zhang, X.J., An, C.B., Zhang, J.W., Zhao, Y., Yu, Z.C., Zhang, R.H., Liu, J.B., Zhou, A.F., Feng, S., 2019. Westerlies Asia and monsoonal Asia: Spatiotemporal differences in climate change and possible mechanisms on decadal to sub-orbital timescales. Earth-Sci. Rev., 192, 337–354.

Chen, J., An, Z., Head, J., 1999. Variation of Rb/Sr ratios in the loesspaleosol sequences of central China during the last 130,000 years and their implications for monsoon paleoclimatology. Quat. Res. 51, 215–219.

Chen, J., Farrell, J. W., Murray, D.W., Prell, W. L., 1995. Timescale and paleoceanographic implications of a 3.6 My oxygen isotope record from the northeast Indian Ocean (Ocean Drilling Program site 758). Paleoceanography 10, 21–47.

Cheng, H., Edwards, R.L., Broecker, W.S., Denton, G.H., Kong, X., Wang, Y., Zhang, R., Wang, X., 2009. Ice age terminations. Science 326, 248–252.

Cheng, H., Edwards, R.L., Sinha, A., Spötl, C., Yi, L., Chen, S., Kelly, M., Kathayat, G., Wang, X., Li, X., Kong, X., Wang, Y., Ning, Y., Zhang, H., 2016. The Asian monsoon over the past 640,000 years and ice age terminations. Nature 534, 640–646.

Cheng, H., Zhang, H., Cai, Y., Shi, Z., Hao, Q., Peng, Y., Sinha, A., Li, H., Zhao, J., Tian, Y., Baker, J., Perez-Mejías, C., 2021. Orbital-scale Asian summer monsoon variations: Paradox and exploration. Sci. China Earth Sci. 64, 529–544. https://doi.org/10.1007/s11430-020-9720-y.

Clark, P.U., Archer, D., Pollard, D., Blum, J.D., Rial, J.A., Brovkin, V., Mix, A.C., Pisias, N.G., Roy, M., 2006. The middle Pleistocene transition, characteristics, mechanisms, and implications for long–term

changes in atmospheric pCO_2. Quat. Sci. Rev. 25, 3150–3184. https://doi.org/10.1016/j.quascirev.2006.07.008.

Clemens, S.C., Holbourn, A., Kubota, Y., Lee, K.E., Liu, Z., Chen, G., Nelson, A., Fox-Kemper, B., 2018. Precession-band variance missing from East Asian monsoon runoff. Nat. Communs. 9, 3364. https://doi.org/10.1038/s41467-018-05814-0.

Clemens, S.C., Kuhnt, W., LeVay, L.J., and the Expedition 353 Scientists, 2016. Indian Monsoon Rainfall. Proceedings of the International Ocean Discovery Program, 353: College Station, TX (International Ocean Discovery Program). http://dx.doi.org/10.14379/iodp.proc.353.2016.

Clemens, S.C., Murray, D.W., Prell, W.L., 1996. Nonstationary phase of the Plio–Pleistocene Asian monsoon. Science 274, 943–948.

Clemens, S.C., Prell, W.L., Murray, D., Shimmield, G., Weedon, G., 1991. Forcing mechanisms of the Indian Ocean monsoon. Nature 353, 720–25.

Clemens, S.C., Prell, W.L., Sun, Y., 2010. Orbital-scale timing and mechanisms driving late Pleistocene Indo-Asian summer monsoons: reinterpreting cave speleothem δ18O. Paleoceanography 25, 1–19.

Clemens, S.C., Prell, W.L., Sun, Y., Liu, Z., Chen, G., 2008. Southern Hemisphere forcing of Pliocene δ18O and the evolution of Indo–Asian monsoons. Paleoceanography 23, 1–15.

Clemens, S.C., Tiedemann, R.F., 1997. Eccentricity forcing of Pliocene-Early Pleistocene climate revealed in a marine oxygen isotope record. Nature 385, 801–804.

Clemens, S.C., Yamamoto, M., Thirumalai, K., Giosan, L., Richey, J.N., Nilsson-Kerr, K., Rosenthal, Y., Anand, P., and McGrath, S.M., 2021. Remote and local drivers of Pleistocene South Asian summer monsoon precipitation: a test for future predictions. Sci. Adv. 7(23), eabg3848. https://doi.org/10.1126/sciadv.abg3848.

Clift, P.D., Hodges, K.V., Heslop, D., Hannigan, R., Long, V.H., Calves, A.G., 2008. Correlation of Himalayan exhumation rates and Asian monsoon intensity. Nat. Geosci. 1, 875–880.

Dash, S., 2005. Monsoons and monsoon climate. In J Oliver (ed.), Encyclopedia of World Climatology. Dordrecht 509–516. Springer.

de Menocal, P., Bloemendal, J., King, J., 1991. A rock–magnetic record of monsoonal dust deposition to the Arabian Sea, Evidence for a shift in the mode of deposition at 2.4 Ma. Proc. ODP: Sci. Res. 117, 389–407. https://doi.org/10.2973/odp.proc.sr.117.178.1991.

Ding, Y, Chan, J., 2005. The East Asian summer monsoon: an overview. Meteorol. Atmos. Phys. 89, 117–42.

Ding, Y.H., Wang, Z.Y., Sun, Y., 2008. Inter-decadal variation of the summer precipitation in East China and its association with decreasing Asian summer monsoon. Part I: Observed evidences. Int. J. Climatol. 28, 1139–1161.

Ding, Z., Derbyshire, E., Yang, S., Sun, J., Liu, T., 2005. Stepwise expansion of desert environment across northern China in the past 3.5 Ma and implications for monsoon evolution. Earth Planet. Sci. Lett. 237, 45–55.

Ding, Z., Derbyshire, E., Yang, S., Yu, Z., Xiong, S., Liu, T., 2002. Stacked 2.6-Ma grain size record from the Chinese loess based on five sections and correlation with the deep-sea $\delta^{18}O$ record. Paleoceanography 17(3).

Ding, Z., Liu, T., Rutter, N.W., Yu, Z., Guo, Z., Zhu, R., 1995. Ice–volume forcing of East Asian winter monsoon variations in the past 800,000 years. Quat. Res. 44, 149–159.

Ding, Z., Ren, J., Yang, S., Liu, T., 1999. Climate instability during the penultimate glaciation, Evidence from two high–resolution loess records, China. J. Geophy. Res. 104, 20123–20132.

Ding, Z., Yu, Z., Rutter, N.W., Liu, T., 1994. Towards an orbital time scale for chinese loess deposits. Quatern. Sci. Rev. 13(1), 39–70.

Elderfield, H., Ferretti, P., Greaves, M., Crowhurst, S., McCave, I.N., Hodell, D.A., Piotrowski, A.M., 2012. Evolution of ocean temperature and ice volume through the mid-Pleistocene climate transition. Science 337, 704–709.

Elderfield, H., Ganssen, G., 2000. Past temperature and δ18O of surface ocean waters inferred from foraminiferal Mg/Ca ratios. Nature 405, 442–445. https://doi.org/10.1038/35013033.

Fang, X., An, Z., Clemens, S.C., Zan, J., Shi, Z., Yang, S., Han, W., 2020. The 3.6-Ma aridity and westerlies history over mid-latitude Asia linked with global climatic cooling, Proc. Natl. Acad. Sci. USA 117, 24729–24734.

Felzer, B., Iii, T.W., Oglesby, R.J., 1998. The impact of ice sheets, CO2, and orbital insolation on late Quaternary climates: sensitivity experiments with a general circulation model. Quat. Sci. Rev. 17, 507–534.

France-Lanord, C., Spiess, V., Klaus, A., Schwenk, T., and the Expedition 354 Scientists, 2016. *Bengal Fan*. Proceedings of the International Ocean Discovery Program, 354: College Station, TX (International Ocean Discovery Program). **http://dx.doi.org/10.14379/iodp.proc.354.2016**

Fu, C., An, Z., Qiang, X., Bloemendal, J., Song, Y., Chang, H., 2013. Magnetostratigraphic determination of the age of ancient Lake Qinghai, and record of the East Asian monsoon since 4.63 Ma. Geology, 41(8), 875–878.

Gai, C., Liu, Q., Roberts, A.P., Chou, Y., Zhao, X., Jiang, Z., and Liu, J., 2020. East Asian monsoon evolution since the late Miocene from the South China Sea. Earth Planet. Sci. Lett. 530, 115960. https://doi.org/10.1016/j.epsl.2019.115960.

Gao, Y.X., Xu, S.Y., Guo, Q.Y., Zhang, M.L., 1962. Some Problems in the East Asian Monsoon. Chinese Science Press, Beijing, pp. 49–87.

Gebregiorgis, D., Hathorne, E.C., Giosan, L., Clemens, S., Nürnberg, D., Frank, M., 2018. Southern Hemisphere forcing of South Asian monsoon precipitation over the past ~1 Million years. Nat. Commun. 9, 4702. https://doi.org/10.1038/s41467-018-07076-2.

Geen, R., Bordoni, S., Battisti, D.S., Hui, K., 2020. Monsoons, ITCZs, and the Concept of the Global Monsoon. Rev. Geophys. 58, e2020RG000700. https://doi.org/10.1029/2020RG000700.

Guo, Z., Berger, A., Yin, Q., Qin, L., 2009. Strong asymmetry of hemispheric climates during MIS-13 inferred from correlating China loess and Antarctica ice records. Clim. Past 5, 21–31.

Guo, Z., Biscaye, P., Wei, L., Chen, X., Peng, S., Liu, T., 2000. Summer monsoon variations over the last 1.2 Ma from the weathering of loess-soil sequences in China. Geophys. Res. Lett. 27(12), 1751–1754.

Guo, Z., Liu, T., Guiot, J., Wu, N., Lu, H., Han, J., Liu, J., Gu, Z., 1996. High frequency pulses of East Asian monsoon climate in the last two glaciations: link with the North Atlantic. Clim. Dyn. 12, 701–709.

Guo, Z.T., Zhou, X., Wu, H.B., 2012. Glacial-interglacial water cycle, global monsoonand atmospheric methane changes. Clim. Dyn. 39, 1073–1092.

Han, W., Fang, X., Berger, A., 2012. Tibet forcing of mid–Pleistocene synchronous enhancement of East Asian winter and summer monsoons revealed by Chinese loess record. Quat. Res. 78, 174–184.

Han, Y., An, Z., Marlon, J.R., Bradley, R.S., Zhan, C., Arimoto, R., Sun, Y., Zhou, W., Wu, F., Wang, Q., Burr, G.S., Cao, J., 2020. Asian inland wildfires driven by glacial–interglacial climate change. Proc. Natl. Acad. Sci. USA 117, 5184–5189. https://doi.org/10.1073/pnas.1822035117.

Hao, Q., Wang, L., Oldfield, F., Peng, S., Qin, L., Song, Y., Xu, B., Qiao, Y., Bloemendal, J., Guo, Z., 2012. Delayed build-up of Arctic ice sheets during 400,000-year minima in insolation variability. Nature 490, 392–396.

Hays, J.D., Imbrie, J., Shackleton, N.J., 1976. Variations in the Earth's orbit, pacemaker of the ice ages. Science 194, 1121–1132.

Head, M.J., Gibbard., P.L., 2015. Early–Middle Pleistocene transitions, linking terrestrial and marine realms. Quat. Int. 389, 7–46. https://doi.org/10.1016/j.quaint.2015.09.042.

Herbert, T.D., Peterson, L.C., Lawrence, K.T., Liu, Z., 2010. Tropical ocean temperatures over the past 3.5 Million years. Science 328, 1530–1534.

Heslop, D., Dekkers, M.J., Langereis, C.G., 2002. Timing and structure of the mid–Pleistocene transition, records from the loess deposits of northern China. Palaeogeogr. Palaeoclimatol. Palaeoecol. 185, 133–143.

Hodell, D.A., Channell, J.E.T., Curtis, J.H., Romero, O., Röhl, U., 2008. Onset of "Hudson Strait" Heinrich Events in the Eastern North Atlantic at the end of the Middle Pleistocene Transition (~640 ka). Paleoceanography 23, PA4218.

Hönisch, B., Hemming, N.G., Archer, D., Siddall, M., McManus, J.F., 2009. Atmospheric carbon dioxide concentration across the mid-Pleistocene transition. Science 324, 1551–1554.

Imbrie, J., Imbrie, K., 1979. Ice Ages: Solving the Mystery. New Jersey: Enslow Publishers, 1–224.

Irino, T., Tada, R., Ikehara, K., Sagawa, T., Karasuda, A., Kurokawa, S., Seki, A., Lu, S., 2018. Construction of perfectly continuous records of physical properties for dark-light sediment sequences collected from the japan sea during integrated ocean drilling program expedition 346 and their potential utilities as paleoceanographic studies. Prog. Earth Planet. Sc. 5(1), 23.

Jansen, J.H.F., Kuijpers, A., Troelstra, S.R., 1986. A mid-Brunhes climatic event: long term changes in global atmosphere and ocean circulation. Science 232, 619–622.

Jian, Z., Huang, B., Kuhnt, W., Lin, H., 2001. Late Quaternary upwelling intensity and East Asian monsoon forcing in the South China Sea. Quat. Res. 55, 363–370.

Jiang, D.B., Wang, H.J., Lang, X.M., 2005. Evaluation of East Asian climatology as simulated by seven coupled models. Adv. Atmos. Sci. 22, 479–495.

Jiang, F., Fu, J., Wang, S., Sun, D., Zhao, Z., 2007. Formation of the Yellow River, inferred from loess-palaeosol sequence in Mangshan and lacustrine sediments in Sanmen gorge, China. Quat. Int. 175(12), 62–70.

Kukla, G., Heller, F., Liu, X.M., Xu, T.C., Liu, T.S., An, Z., 1988. Pleistocene climate in China dated by magnetic susceptibility. Geology 16, 811–814.

Kunkelova, T., Jung, S.J.A., de Leau, E.S., Odling, N., Thomas, A.L., Betzler, C., Eberli, G.P., Alvarez-Zarikian, C.A., Alonso-García, M., Bialik, O.M., Blättler, C.L., Guo, J.A., Haffen, S., Horozal, S., Mee, A.L.H., Inoue, M., Jovane, L., Lanci, L., Laya, J.C., Lüdmann, T., Bejugam, N.N., Nakakuni, M., Niino, K., Petruny, L.M., Pratiwi, S.D., Reijmer, J.J.G., Reolid, J., Slagle, A.L., Sloss, C.R., Su, X., Swart, P.K., Wright, J.D., Yao, Z., Young, J.R., Lindhorst, S., Stainbank, S., Rueggeberg, A., Spezzaferri, S., Carrasqueira, I., Yu, S., and Kroon, D., 2018. A two million year record of low-latitude aridity linked to continental weathering from the Maldives. Prog. Earth Planet. Sc 5(1), 86. https://doi.org/10.1186/s40645-018-0238-x.

Kutzbach, J.E., Guetter, P.J., 1986. The influence of changing orbital parameters and surface boundary conditions on climate simulations for the past 18 000 years. J. Atmos. Sci. 43, 1726–59.

Kutzbach, J.E., Liu, X., Liu, Z., Chen, G., 2008. Simulation of the evolutionary response of global summer monsoons to orbital forcing over the past 280,000 years. Clim. Dyn. 30, 567–579. https://doi.org/10.1007/s00382-007-0308-z.

Kutzbach, J.E., Otto-Bliesner, B.L., 1982. The Sensitivity of the African-Asian Monsoonal Climate to Orbital Parameter Changes for 9000 Years B.P. in a Low-Resolution General Circulation Model. J. Atmos. Sci. 39, 1177–1188.

Lee, J., Kim, S., and Khim, B.-K., 2020. A paleoproductivity shift in the northwestern Bay of Bengal (IODP Site U1445) across the mid-Pleistocene transition in response to weakening of the Indian summer monsoon. Palaeogeogr. Palaeoclimatol. Palaeoecol. 560:110018.

https://doi.org/10.1016/j.palaeo.2020.110018.

Lei, Y.H., Hoskins, B., Slingo, J., 2014. Natural variability of summer rainfall over China in HadCM3. Clim. Dyn. 42, 417–432.

Li, B., Feng, Q., Wang, F., Wang, X., Li, R., 2019. A 1.68 Ma organic isotope record from the hetao basin, upper reaches of the Yellow River in northern China: implications for hydrological and ecological variations. Glob. Planet. Change 184, 103061.

Li, J., Fang, X., Song, C., Pan, B., Ma, Y., Yan, M., 2014. Late Miocene–Quaternary rapid stepwise uplift of the NE Tibetan Plateau and its effects on climatic and environmental changes. Qua. Res. 81, 400–423.

Li, L., Li, Q., Tian, J., Wang, P., Wang, H., Liu, Z., 2011. A 4–Ma record of thermal evolution in the tropical western Pacific and its implications on climate change. Earth Planet. Sci. Lett. 309, 10–20.

Li, M., Hinnov, L., Kump, L., 2019. Acycle: Time-series analysis software for paleoclimate research and education. Comput. Geosci. 127, 12–22. https://doi.org/10.1016/j.cageo.2019.02.011.

Li, T. and Li, G., 2014. Incorporation of trace metals into microcodium as novel proxies for paleo–precipitation. Earth Planet. Sci. Lett. 386, 34–40. https://doi.org/10.1016/j.epsl.2013.10.011.

Li, T., Liu, F., Abels, H. A., You, C., Zhang, Z., Chen, J., Ji, J., Li, L., Li, L., Liu, H., Ren, C., Xia, R., Zhao, L., Zhang, W., Li, G., 2016. Continued obliquity pacing of East Asian summer precipitation after the mid–Pleistocene transition. Earth Planet. Sci. Lett. 457, 181–190. https://doi.org/10.1016/j.epsl.2016.09.045.

Li, Y., Lu, R.Y., Dong, B.W., 2007. The ENSO–Asian monsoon interaction in acoupled ocean–atmosphere GCM. J. Clim. 20, 5164–5177.

Lisiecki, L.E., Raymo, M.E., 2005. A Pliocene–Pleistocene stack of 57 globally distributed benthic δ18O records. Paleoceanography 20, 1–17.

Liu, J., Liu, Q., Zhang, X., Liu, J., Wu, Z., Mei, X., Shi, X., Zhao, Q., 2016. Magnetostratigraphy of a long Quaternary sediment core in the south Yellow Sea. Quat. Sci. Rev. 144, 1–15.

Liu, T, Ding, Z., 1998. Chinese loess and the paleomonsoon. Annu. Rev. Earth Planet. Sci. 26, 111–145.

Liu, T., Ding, Z., Rutter, N., 1999. Comparison of Milankovitch periods between continental loess and deep sea records over the last 2.5 Ma. Quat. Sci. Rev. 18, 1205–1212. https://doi.org/S0277-3791(98)00110-3.

Liu, W., Liu, Z., Sun, J., Song, C., Chang, H., Wang, H., Wang, Z., An, Z., 2020. Onset of permanent Taklimakan Desert linked to the mid-Pleistocene transition. Geology 48, 782–786.

Liu, W., Yang, H., Sun, Y., Wang, X., 2011. $\delta^{13}C$ values of loess total carbonate, a sensitive proxy for Asian summer monsoon in arid northwestern margin of the Chinese loess plateau. Chem. Geol. 284, 317–322. https://doi.org/10.1016/j.chemgeo.2011.03.011.

Liu, Z., Wen, X., Brady, E.C., Otto–Bliesner, B., Yu, G., Lu, H., Cheng, H., Wang, Y., Zheng, W., Ding, Y., Edwards, R.L., Cheng, J., Liu, W., Yang, H., 2014. Chinese cave records and the East Asia summer monsoon. Quat. Sci. Rev. 83, 115–128.

Lu, H,X,, Liu, W.G., Yang, H., Wang, H.Y., Liu, Z.H., Leng, Q., Sun, Y.B., Zhou, W.J., An, Z.S., 2019. 800-kyr land temperature variations modulated by vegetation changes on Chinese Loess Plateau. Nat. Commun. 10, 1530–1534.

Lu, H., Liu, X., Zhang, F., An, Z., Dodson, J., 1999. Astronomical calibration of loess–paleosol deposits at Luochuan, central Chinese loess plateau. Palaeogeogr. Palaeoclimatol. Palaeoecol. 154, 237–246. https://doi.org/10.1016/S0031-0182(99)00113-3.

Lü, H., Wang, S., Wu, N., Tong, G., Yang, X., Shen, C., Li, S., Zhu, L. Wang, L., 2001. A new pollen record of the last 2.8 Ma fromthe Co Ngoin, central Tibetan Plateau. Sci. China Ser. D 44 (Supp.), 292–300.

Lu, H., Wang, X., Wang, X., Sun, X., Yi, S., Zhou, Y., Liu, Q., Swinehart, J., Vandenberghe, J., 2012. Palaeoclimatic changes in northeastern Qinghai-Tibetan Plateau revealed by magnetostratigraphy and magnetic susceptibility analysis of thick loess deposits, Neth. J. Gersci. (Geologie en Mijnbouw) 91(1–2), 189–198.

Lu, H., Yi, S., Liu, Z., Mason, J.A., Jiang, D., Cheng, J., Stevens, T., Xu, E., Jin, L., Zhang, Z., Guo, Z., Wang, Y., Otto–Bliesner, B., 2013. Variation of East Asian monsoon precipitation during the past 21 k.y. and potential CO_2 forcing. Geology 41, 1023–1026.

Lu, H., Zhang, F., Liu, X., Duce, R.A., 2004. Periodicities of palaeoclimatic variations recorded by loess–paleosol sequences in China. Quat. Sci. Rev. 23, 1891–1900.

Lyu, A., Yin, Q., Crucifix, M., Sun, Y., 2021. Diverse regional sensitivity of summer precipitation in East Asia to ice volume, CO_2 and astronomical forcing. Geophys. Res. Lett. 48, e2020GL092005. https://doi.org/10.1029/2020GL092005.

Maher, B.A., 2016. Palaeoclimatic records of the loess/palaeosol sequences of the Chinese Loess Plateau. Quat. Sci. Rev. 154, 23–84.

Maher, B.A., Thompson, R., 1995. Paleorainfall reconstructions from pedogenic magnetic susceptibility variations in the Chinese loess and paleosols. Quat. Res. 44, 383–391.

McClymont, E.L., Rosell–Melé, A., Haug, G., Lloyd, J.M., 2008. Expansion of subarctic water masses in the North Atlantic and Pacific oceans and implications for mid-Pleistocene ice sheet growth. Paleoceanography 23, 1–12. https://doi.org/10.1029/2008pa001622.

Miao, Y., Warny, S., Liu, C., Clift, P.D., Gregory, M., 2017. Neogene fungal record from IODP site U1433, south China Sea: implications for paleoenvironmental change and the onset of the Mekong River. Mar. Geol. 394, 69–81.

Milankovitch, M., 1941. Canon of insolation and the ice–age problem. R. Serb. Acad. Spec. Publ. (translated by the Israel Program for Scientific Translations, Jerusalem, 1969).

Müller, P.J., Kirst, G., Ruhland, G., Storch, I.V., Rosell-Mele, A., 1998. Calibration of the Alkenone paleotemperature index UK37 based on core-tops from the eastern South Atlantic and the global ocean (60° N–60° S). Geochim. Cosmochim. Acta 62, 1757–1772.

Naafs, B.D.A., Hefter, J., Stein, R., 2013. Millennial-scale ice rafting events and Hudson Strait Heinrich (-like) events during the late Pliocene and Pleistocene: a review. Quat. Sci. Rev. 80, 1–28.

Nie, J., Stevens, T., Rittner, M., Stockli, D., Garzanti, E., Limonta, M., Bird, A., Ando, S., Vermeesch, P., Saylor, J., Lu, H., Breecker, D., Hu, X., Liu, S., Resentini, A., Vezzoli, G., Peng, W., Carter, A., Ji, S., Pan, B., 2015, Loess Plateau storage of Northeastern Tibeta Plateau-derived Yellow River sediment. Nat. Commun. 6, 8511 (2015).

Pandey, D.K., Clift, P.D., Kulhanek, D.K., and the Expedition 355 Scientists, 2016. Arabian Sea Monsoon. Proceedings of the International Ocean Discovery Program, 355: College Station, TX (International Ocean Discovery Program). http://dx.doi.org/10.14379/iodp.proc.355.2016.

Peterse, F., Martínez-García, A., Zhou, B., Beets, C.J., Prins, M.A., Zheng, H., Eglintonet, T.I., 2014. Molecular records of continental air temperature and monsoon precipitation variability in East Asia spanning the past 130,000 years. Quat. Sci. Rev. 83, 76–82.

Petit, J.R., Jouzel, J., Raynaud, D., Barkov, N., Barnola, J.M., Basile, I., Bender, M., Chappellaz, J., Davisk, M., Delaygue, G., Delmotte, M., Kotlyakov, V.M., Legrand, M., Lipenkov, V.Y., Lorius, C., Pepin, L., Riz, C., Saltzmank, E., Stievenard, M., 1999. Climate and atmospheric history of the past 420,000 years from the Vostok ice core, Antarctica. Nature 399, 429–36.

Pisias, N.G., Moore, T.C., 1981. The evolution of Pleistocene climate, a time series approach. Earth Planet. Sci. Lett. 52, 450–458.

Prell, W.L., Kutzbach, J.E., 1987. Monsoon variability over the past 150,000 years. J. Geophys. Res. 92, 8411–8425.

Prell, W.L., Kutzbach, J.E., 1992. Sensitivity of the Indian monsoon to forcing parameters and implications for its evolution. Nature 360, 647–652.

Rao, Z., Chen, F., Cheng, H., Liu, W, Wang, G., Lai, Z., Bloemendal, J., 2013. High-resolution summer precipitation variations in the western Chinese loess plateau during the last glacial. Sci. Rep. 3, 2875.

Rao, Z., Zhu, Z., Chen, F., Zhang, J., 2006. Does δ13Ccarb of the Chinese loess indicate past C3/C4 abundance? a review of research on stable carbon isotopes of the Chinese loess. Quat. Sci. Rev. 25, 2251–2257.

Raymo, M.E., Oppo, D.W., Curry, W., 1997. The mid–Pleistocene climate transition: A deep sea carbon isotopic perspective. Paleoceanography 12, 546–559.

Rits, D.S., Prins, M.A., Troelstra, S.R., Balen, R.T.V., Zheng, Y., Beets, C.J., Wang, B., Li, X., Zhou, J., Zheng, H., 2016. Facies analysis of the middle and late quaternary sediment infill of the northern weihe basin, central china. J. Quaternary Sci. 31, 152–165.

Rohling, E.J., 2007. Progress in paleosalinity: Overview and presentation of a new approach. Paleoceanography 22, PA3215.

Rohling, E.J., Foster, G.L., Grant, K.M., Marino, G., Roberts, A.P., Tamisiea, M.E., Williams, F., 2014. Sea–level and deep–sea–temperature variability over the past 5.3 million years. Nature 508, 477–482.

Ruddiman, W.F., Raymo, M., McIntyre, A., 1986. Matuyama 41,000-year cycles: North Atlantic Ocean and northern hemisphere ice sheets. Earth Planet. Sci. Lett. 80, 117–129.

Shackleton, N.J., 2000. The 100,000–year ice–age cycle identified and found to lag temperature, carbon dioxide, and orbital eccentricity. Science 289, 1897–1902.

Shen, C., Tang, L., Wang, S., Li, C., Liu, K.B., 2005. Pollen records and time scale for the RM core of the Zoige Basin, northeastern Qinghai-Tibetan Plateau. Chin. Sci. Bull. 50, 553–562.

Shen, J., Lu, H., Wang, S., Chen, S., Yang, X., Wu, Y., Zhu, Z., 2004. A 2.8 Ma record of environmental evolution and tectonic events inferred from the Cuoe core in the middle of Tibetan Plateau. Sci China Ser D. 47 (11), 1025–1034.

Shen, J., Xiao, H., Wang, S., An, Z., Qiang, X., Xiao, X., 2007. The orbital scale evolution of regional climate recorded in a long sediment core from Heqing, China. Chinese Sci. Bull. 52, 1813–1819.

Shi, F., Yin, Q.Z., Nikolova, I., Berger, A., Ramstein, G., Guo, Z.T., 2021. Impacts of extremely asymmetrical polar ice sheets on the East Asian summer monsoon during the MIS-13 interglacial. Quat. Sci. Rev. 231, 106164.

Shi, X., Yao, Z., Liu, Q., Larrasoaña, J.C., Bai, Y., Liu, Y., Liu, J., Cao, P., Li, X., Qiao, S., Wang, K., Fang, X., Xu, T., 2016. Sedimentary architecture of the bohai sea china over the last 1 ma and implications for sea-level changes. Earth Planet. Sci. Lett. 451, 10–21.

Shi, Z.G., Liu, X.D., Sun, Y.B., An, Z.S., Liu, Z.Y., Kutzbach J., 2011. Distinct responses of East Asian summer and winter monsoons to orbital forcing. Clim past, 7, 1363-1370.

Song, Y., Fang, X., King, J.W., Li, J., Naoto, I., An, Z., 2014. Magnetic parameter variations in the Chaona loess/paleosol sequences in the central Chinese Loess Plateau, and their significance for the middle Pleistocene climate transition. Quat. Res. 81, 433–444.

Sun J., Liu T., 2000a. Stratigraphic evidence for the uplift of the Tibetan Plateau between ~1.1 and ~0.9 Myr ago. Quat. Res. 54, 309–320.

Sun J., Liu T., 2000b. Multiple origins and interpretations of the magnetic susceptibility signal in Chinese wind-blown sediments. Earth Planet. Sci. Lett. 180, 287–296.

Sun, J., 2005. Long-termfluvial archives in the Fen Wei Graben, central China, and their bearing on the tectonic history of the India–Asia collision system during the Quaternary. Quat. Sci. Rev. 24, 1279–1286.

Sun, Y., An, Z., Clemens, S.C., Bloemendal, J., Vandenberghe, J., 2010. Seven million years of wind and precipitation variability on the Chinese Loess Plateau. Earth Planet. Sci. Lett. 297, 525–535.

Sun, Y., Clemens, S.C., An, Z., Yu, Z., 2006a. Astronomical timescale and palaeoclimatic implication of stacked 3.6–Myr monsoon records from the Chinese Loess Plateau. Quat. Sci. Rev. 25, 33–48.

Sun, Y., Chen, J., Clemens, S.C., Liu, Q., Ji, J., Tada, R., 2006b. East Asian monsoon variability over the last seven glacial cycles recorded by a loess sequence from the northwestern Chinese Loess Plateau. Geochem. Geophys. Geosys. 7, Q12Q02.

Sun, Y., Kutzbach, J., An, Z., Clemens, S., Liu, Z., Liu, W., Liu, X., Shi, Z., Zheng, W., Liang, L., Yan, Y., 2015. Astronomical and glacial forcing of East Asian summer monsoon variability. Quat. Sci. Rev. 115, 132–142. https://doi.org/10.1016/j.quascirev.2015.03.009.

Sun, Y., McManus, J.F., Clemens, S.C., Zhang, X., Vogel, H., Hodel, D.A., Guo, F., Wang, T., Liu, X., An, Z., 2021. Persistent orbital influence on millennial climate variability through the Pleistocene. Nat. Geosci. https://doi.org/10.1038/s41561-021-00794-1.

Sun, Y., Yin, Q., Crucifix, M., Clemens, S.C., Araya–Melo, P., Liu, W., Qiang, X., Liu, Q., Zhao, H., Liang, L., Chen, H., Li, Y., Zhang, L., Dong, G., Li, M., Zhou, W., Berger, A., An, Z., 2019. Diverse manifestations of the mid–Pleistocene climate transition. Nat. Communs. 10, 1–11.

Tada, R., I. Koizumi, A. Cramp, and A. Rahman, 1992. Correlation of dark and light layers, and the origin of their cyclicity in the Quaternary sediments from the Japan Sea, Proc. Ocean Drill. Progr., Sci. Res., 127/128, 577–601.

Tada, R., Irino, T., Ikehara, K., Karasuda, A., Sugisaki, S., Xuan, C., Sagawa, T., Itaki, T., Kubota, Y., Lu, S., Seki, A., Murray, R.W., Alvarez-Zarikian, C., Anderson, W.T., Bassetti, M.-A., Brace, B.J., Clemens, S.C., da Costa Gurgel, M.H., Dickens, G.R., Dunlea, A.G., Gallagher, S.J., Giosan, L., Henderson, A.C.G., Holbourn, A.E., Kinsley, C.W., Lee, G.S., Lee, K.E., Lofi, J., Lopes, C.I.C.D., Saavedra-Pellitero, M., Peterson, L.C., Singh, R.K., Toucanne, S., Wan, S., Zheng, H., Ziegler, M., 2018. High-resolution and high-precision correlation of dark and light layers in the Quaternary hemipelagic sediments of the Japan Sea recovered during IODP Expedition 346. Prog. Earth Planet. Sc. 5(1), 19.

Tada, R., Murray, R.W., Alvarez Zarikian, C.A., and the Expedition 346 Scientists, 2015. Proceedings of the International Ocean Discovery Program, 346: College Station, TX (Integrated Ocean Drilling Program). https://doi.org/10.2204/iodp.proc.346.2015.

Tian, J., Wang, P., Cheng, X., Li, Q., 2002. Astronomically tuned Plio–Pleistocene benthic δ18O record from South China Sea and Atlantic–Pacific comparison. Earth Planet. Sci. Lett. 203, 1015–1029.

Tian, J., Xie, X., Ma, W., Jin, H., Wang, P., 2011. X–ray fluorescence core scanning records of chemical weathering and monsoon evolution over the past 5 Myr in the southern South China Sea. Paleoceanography 26, 1–17.

Thomas, E.K., Clemens. S.C., Sun, Y.B., Prell, W.L., Huang, Y., Gao, L., Loomis, S., Chen, G., Liuet, Z., 2016. Heterodynes dominate precipitation isotopes in the East Asian monsoon region, reflecting interaction of multiple climate factors. Earth Planet. Sci. Let. 455, 196–206.

Wang, B., 2006. The Asian Monsoon. Springer/Praxis, New York, 787.

Wang, B., Ding, Q., 2008. Global monsoon: dominant mode of annual variation in the tropics. Dyn. Atmos. Oceans 44, 165–183.

Wang, J., Fang, X., Appel, E., Song, C., 2012. Pliocene-Pleistocene climate change at the NE Tibetan Plateau deduced from lithofacies variation in the drill core SG-1, western Qaidam Basin, China. J. Sed. Res. 82, 933–952.

Wang, P., Jian, Z., Zhao, Q., Li, Q., Wang, R., Liu, Z., Wu, G., Shao, L., Wang, J., Huang, B., Fang, D., Tian, J., Li, J., Li, X., Wei, G., Sun, X., Luo, Y., Su, X., Mao, S., Chen, M., 2003. Evolution of the South China Sea and monsoon history revealed in deep-sea records. Chinese Sci. Bull. 48, 2549–2561.

Wang, P.X., Clemens, S., Beaufort, L., Braconnot, P., Dickens, G.R., Huber, M., Jian, Z.M., Kershaw, P., Sarnthein, M., 2005. Evolution and variability of the Asian monsoon system: state of the art and outstanding issues. Quat. Sci. Rev. 24, 595–629.

Wang, P., Prell, W.L., Blum, P., and Shipboard Scientific Party, 2000. Proceedings of the Ocean Drilling Program, Initial Reports, 184: College Station, TX (Ocean Drilling Program). http://doi.org/10.2973/odp.proc.ir.184.106.2000

Wang, P., Wang, B., Cheng, H., Fasullo, J., Guo, Z., Kiefer, T., Liu, Z., 2014. The global monsoon across timescales, coherent variability of regional monsoons. Clim. Past 10, 2007–2052.

Wang, P., Wang, B., Cheng, H., Fasullo, J., Guo, Z., Kiefer, T., Liu, Z., 2017. The global monsoon across time scales, mechanisms and outstanding issues. Earth Sci. Rev. 174, 84–121. https://dx.doi.org/10.1016/j.earscirev.2017.07.006.

Wang, Y., Cheng, H., Edwards, R., An, Z., Wu, J., Shen, C., Dorale, J., 2001. A high-resolution absolute-dated late Pleistocene monsoon record from Hulu Cave, China. Science 294, 2345–2348.

Wang, Y., Cheng, H., Edwards, R.L., Kong, X., Shao, X., Chen, S., Wu, J., Jiang, X., Wang, X., An, Z., 2008. Millennial–and orbital–scale changes in the East Asian monsoon over the past 224,000 years. Nature 451, 1090–1093.

Webster, P.J., Magana, V.O., Palmer, T.N., Shukla, J., Tomas, R.A., Yanai, M.U., Yasunari, T., 1998. Monsoons, processes, predictability, and the prospects for prediction. J. Geophys. Res. Oceans 103, 14451–14510.

Wehausen, R., Brumsack, H., 2002. Astronomical forcing of the East Asian monsoon mirrored by the composition of Pliocene South China Sea sediments, Earth Planet. Sci. Lett. 201, 621–636.

Wei, G., Li X., Liu Y., Shao L., Liang X., 2006. Geochemical record of chemical weathering and monsoon climate change since the early Miocene in the South China Sea, Paleoceanography 21, PA4214.

Wen, X., Liu, Z., Wang, S., Cheng, J., Zhu, J., 2016. Correlation and anti-correlation of the East Asian summer and winter monsoons during the last 21,000 years. Nat. Communs. 7, 11999. https://doi.org/10.1038/ncomms11999.

Williams, D.F., Kuzmin, M.I., Prokopenko, A.A., Karabanov, E.B., Khursevich, G.K., Bezrukova, E.V., 2001. The Lake Baikal drilling project in the context of a global lake drilling initiative. Quat. Int. 80, 3–18. https://doi.org/10.1016/S1040-6182(01)00015-5.

Xiao, J., An, Z., 1999. Three large shifts in East Asian monsoon circulation indicated by loess–paleosol sequences in China and late Cenozoic deposits in Japan. Palaeogeogr. Palaeoclimatol. Palaeoecol. 154, 179–189.

Xiao, J., Zheng, H., Zhao, H., 1992. Variation of winter monsoon intensity on the Loess Plateau, central China during the last 130,000 years, evidences from grain size distribution. Quat. Res. 31, 13–19.

Xin, S., Shen, J., Zhang, W., Sun, W., Xiao, X., 2019. East Asian winter monsoon evolution since the late Pliocene based on a pollen record from Lake Xingkai, northeast Asia. Quat. Res. 93, 40–59.

Xiong, S., Ding, Z., Liu, T., 2001. Climatic implications of loess deposits from the Beijing region. J. Quat. Sci. 6, 575–582.

Yang, S., Ding, Z., Li, Y., Wang, X., Jiang, W., Huang, X., 2015. Warming-induced northwestward migration of the east Asian monsoon rain belt from the last glacial maximum to the mid-holocene. P. Natl. Acad. Sci. USA 112, 13178–13183.

Yao, Z., Guo, Z., Xiao, G., Wang, Q., Shi, X., and Wang, X. (2012). Sedimentary history of the western Bohai coastal plain since the late Pliocene: implications on tectonic, climatic and sea-level changes. J. Asian Earth Sci. 54–55, 192–202. https://doi. org/10.1016/j.jseaes.2012.04.013.

Yi, L., Deng, C., Tian, L., Xu, X., Jiang, X., Qiang, X., Qin, H., Ge, J., Chen, G., Su, Q., Chen, Y., Shi, X., Xie, Q., Yu, H., Zhu, R., 2016. Plio-Pleistocene evolution of Bohai basin (East Asia): demise of Bohai

Paleolake and transition to marine environment. Sci. Rep. 6:29403.

Yin, Q., Berger, A., Crucifix, M., 2009. Individual and combined effects of ice sheets and precession on MIS-13 climate. Clim. Past 5, 229–243.

Yin, Q., Berger, A., Driesschaert, E., Goosse, H., Loutre, M.F., Crucifix, M., 2008. The eurasian ice sheet reinforces the East Asian summer monsoon during the interglacial 500 000 years ago. Clim. Past 4(2), 80-90.

Zachos, J., Pagani, M., Sloan, L., Thomas, E., Billups, K., 2001. Trends, rhythms, and aberrations in global climate 65 Ma to present. Science 292, 686–93.

Zeng, L., Lu, H., Yi, S., Li, Y., Lv, A., Zhang, W., Xu, Z., Wu, H., Feng, H., Cui, M., 2016. New magnetostratigraphic and pedostratigraphic investigations of loess deposits in north-east china and their implications for regional environmental change during the mid-pleistocene climatic transition. J. Quat. Sci. 31(1), 20–32.

Xhang, H.B., Griffiths, M.L., Chiang, J.C.H., Kong, W.W., Wu, S.T., Atwood, A., Huang, J.H., Cheng, H., Ning, Y.F., Xie, S.C., 2018. East Asian hydroclimate modulated by the position of the westerlies during Termination I. Science 362, 580–583.

Zhang, H.B., Nie, J.S., Liu, X.J., Pullen, A., Li, G.Q., Peng, W.B., Zhang, H.Z., 2021. Spatially variable provenance of the Chinese Loess Plateau. Geology 49(10): 1155-1159

Zhang, J., Li, J., Guo, B., Ma, Z., Li, X., Ye, X., Yu, H., Liu, J., Yang, C., Zhang, S., Song, C., Hui, Z., Peng, T., 2016. Magnetostratigraphic age and monsoonal evolution recorded by the thickest quaternary loess deposit of the Lanzhou region, western Chinese Loess Plateau. Quat. Sci. Rev. 139, 17–29.

Zhang, W., Appel, E., Fang, X., Yan, M., Song, C., Cao, L., 2012. Paleoclimatic implications of magnetic susceptibility in late pliocene-quaternary sediments from deep drilling core sg-1 in the western qaidam basin (ne tibetan plateau). J. Geophy. Res–Sol. Ea. 117, B06101.

Zhang, W., De, Vleeschouwer, D., Shen, J., Zhang, Z., Zeng, L., 2018. Orbital time scale records of asian eolian dust from the Sea of Japan since the early pliocene. Quat. Sci. Rev. 187, 157–167.

Zhang, Y., Ji, J., Balsam, W.L., Liu, L., Chen, J., 2007. High resolution hematite and goethite records from ODP 1143, South China Sea, co–evolution of monsoonal precipitation and El Niño over the past 600,000 years. Earth Planet. Sci. Lett. 264, 136–150.

Zhang, Y., Ji, J., Balsam, W.L., Liu, L., Chen, J., 2009. Mid–Pliocene Asian monsoon intensification and the onset of Northern Hemisphere glaciation. Geology 37, 599–602.

Zhao, Y., Tzedakis, P.C., Li, Q., Qin, F., Cui, Q., Liang, C., Birks, H.B., Liu, Y.L., Zhang, Z.Y., Ge, J.Y., Zhao, H., Felde, V.A., Deng, C.L., Cai, M.T., Li, H., Ren, W.H., Wei, H.C.,Yang, H.F., Zhang, J.W., Yu, Z.C., Guo, Z., 2020. Evolution of vegetation and climatevariability on the Tibetan Plateau over the past 1.74 million years. Sci. Adv. 6, eaay6193.

Zheng, H., An, Z., Shaw, J., 1992. New contributions to Chinese Plio-Pleistocene magnetostratigraphy. Phys. Earth Planet. Inter. 70, 146–153.

Zheng, H., Huang, X., Ji, J., Rui, L., Zeng, Q., Jiang, F., 2007. Ultra-high rates of loess sedimentation at zhengzhou since stage 7: implication for the yellow river erosion of the sanmen gorge. Geomorphology 85(3–4), 131–142.

Zhou, L., Oldfield, F., Wintle, A.G., Robinson, S.G., Wang, J., 1990. Partly pedogenic origin of magnetic variations in Chinese loess. Nature 346, 737–739.

Ziegler, M., Lourens, L.J., Tuenter, E., Hilgen, F., Reichart, G.J., Weber, N., 2010. Precession phasing offset between Indian summer monsoon and Arabian Sea productivity linked to changes in Atlantic overturning circulation. Paleoceanography 25, PA3213, 1–16. https://doi.org/10.1029/2009PA001884.

Table 1. Lists of Quaternary paleoclimatic records in East Asia and its surrounding oceans.

Archives	Sites	Location	Proxies	Time span (Ma)	References
Loess	Chashmanigar	38.38°N, 69.82°E	Median, MS, a*, $\delta^{13}C_{OC}$	0-1.77	Ding et al., 2002a; Yang et al., 2006
	Kunlun	36.20°N, 81.34°E	>30 μm, >30 μm flux	0-3.6	Fang et al., 2020
	Lop Nor	39.77°N, 88.38°E	Mode, MS, $\delta^{13}C_{IC}$	0-7.1	Chang et al., 2012; Liu et al., 2020
	Gulang	37.49° N, 102.88° E	Mean, Fe/K	0-1.5	Sun et al., 2021
	Xining	36.51°N, 101.73°E	MS	0-2	Lu et al., 2012
	Lanzhou	36.00° N, 103.83° E	Median, MS	0-2.2	Chen et al., 1991; Zhang et al., 2016
	Jingyuan	36.35°N, 104.60°E	Mean, MS, $\delta^{13}C_{IC}$	0-1.7	Sun et al., 2019
	Jingbian	37.68° N, 108.52° E	Median, MS	0-3.5	Ding et al., 2005
	Xifeng	35.75°N, 107.82°E	Quartz Mean, MS	0-7.5	Kukla et al., 1988; Sun et al., 2006a
	Jingchuan	35.29°N, 107.37°E	Median, MS	0-7.2	Ding et al., 2002b
	Chaona	35.17°N, 107.20°E	>30 μm, MS	0-2.6	Song et al., 2014
	Changwu	35.20°N, 107.70°E	MS, MS_{FD}, FeD/FeT	0-1.2	Guo et al., 2000
	Lingtai	35.07°N, 107.65°E	Quartz Mean, MS	0-7.2	Ding et al., 1999; Sun et al., 2006a
	Luochuan	35.75°N, 109.42°E	Mean, MS	0-2.6	An et al., 1990; Xiao and An, 1999; Han et al., 2020
	Puxian	36.44°N, 110.89°E	Median	0-2.6	Ding et al., 2002b
	Baoji	34.20°N, 107.00°E	Median	0-2.6	Ding et al., 1994, 2002b
	Lantian	34.18°N, 109.23°E	MS, $\delta^{13}C_{IC}$, Rb/Sr	0-5	Zheng et al., 1992; An et al., 2005; Bloemendal et al., 2008
	Weinan	34.35° N, 109.52° E	MS	0-2.6	Sun, 2005
	Mangshan	34.95° N, 113.36° E	Median, MS	0-1.1	Jiang et al., 2007; Zheng et al., 2007
	Fanshan	40.50°N, 115.17°E	Median, MS	0-1.1	Xiong et al., 2001
	Chifeng	42.31°N, 118.69°E	MS	0-1.2	Zeng et al., 2016
Speleothem	Hulu	32.50°N, 119.17°E	$\delta^{18}O$	0-0.075	Wang et al., 2001
	Sanbao	31.67°N, 110.43°E	$\delta^{18}O$	0-0.64	Wang et al., 2008; Cheng et al., 2016
	Xiaobailong	24.20°N, 103.35°E	$\delta^{18}O$	0-0.25	Cai et al., 2015
	Kesang	42.87°N, 81.75°E	$\delta^{18}O$	0-0.5	Cheng et al., 2012
Lake	Baikal	53.70°N, 108.51°E	BioSi, MS	0-3.6	BDP Members, 1997; Prokopenko et al., 2006
	Xingkai	45.31°N, 132.58°E	Pollen	0-3.6	Xin et al., 2019
	SG1	38.20°N, 92.51°E	MS	0-2.77	Wang et al., 2012; Zhang et al., 2012
	SG3	38.38°N, 91.75°E	Mean, Pollen	0-3.1	Cai et al., 2012
	Cuoe	31.52°N, 91.55°E	Pollen, Median, Rb/Sr	0-2.8	Lü et al., 2001; Shen et al., 2004
	Qinghai	36.67°N, 100.38°E	Mean	0-5.1	Fu et al., 2013
	Zoige	33.97°N, 102.33°E	Arboreal pollen	0-1.7	Zhao et al., 2020
	Hetao	40.75°N, 108.39°E	Mean, TOC,C/N	0-1.7	Li et al., 2020
	Luyang	34.82°N, 109.53°E	Median, $CaCO_3$	0-1.1	Rits et al., 2016
	Heqing	26.57°N, 100.17°E	*Tsuga*, ISM index	0-2.6	An et al., 2011
Coastal Zone Marginal Seas	BZ2	39.02°N, 117.13°E	a*, b*	0-3.3	Yao et al., 2012
	BH8	38.28°N, 119.99°E	a*, b*, S/Cl	0-1.06	Shi et al., 2016
	CSDP1	34.30°N, 122.37°E	M_{rs}/MS	0-3.5	Liu et al., 2016
	U1429	31.62°N, 129.00°E	$\delta^{18}O_b$, $\delta^{18}O_p$, MS, L*, a*, b*	0-0.04	Tada et al., 2015; Clemens et al., 2018
Japan Sea	U1422	43.77°N, 138.83°E	K, MS, L*, a*, b*	0-3.9	Tada et al., 2015; Zhang et al., 2018
	U1423	41.70°N, 139.08°E	MS, L*, a*, b*	0-5	Tada et al., 2015; Irino et al., 2018
	U1424	40.19°N, 138.23°E	MS, L*, a*, b*	0-4	Tada et al., 2015, 2018
	U1425	39.50°N, 134.45°E	MS, L*, a*, b*	0-10	Tada et al., 2015
	U1426	37.03°N, 134.80°E	MS, L*, a*, b*	0-5	Tada et al., 2015
	U1427	35.97°N, 134.43°E	MS, L*, a*, b*	0-1.4	Tada et al., 2015
	U1430	37.90°N, 131.54°E	MS, L*, a*, b*	0-15	Tada et al., 2015
South China Sea	1143	9.36°N, 113.29°E	$\delta^{18}O_b$, SST, Ti/Al, Hm/Gt	0-5	Tian et al., 2002, 2011; Zhang et al., 2009; Li et al., 2011
	1145	19.58°N, 117.63°E	$\delta^{18}O_p$, MS, L*, a*, b*	0-3.5	Wang et al., 2000, 2003; Boulay et al., 2005
	1146	19.45°N, 116.27°E	$\delta^{18}O_b$, $\delta^{18}O_p$, SST, Ba/Al	0-5	Clemens et al., 2008; Herbert et al., 2010
	1148	18.84°N, 116.57°E	$\delta^{18}O_p$	0-6	Wang et al., 2003; Jian et al., 2001
	U1431	15.38°N, 117.00°E	MS, Hm/Gt	0-6.5	Gai et al., 2020
	U1433	12.37°N, 115.05°E	Fungal spore	0-17	Miao et al., 2017
Bay of Bengal	758	5.38°N, 90.35°E	$\delta^{18}O_b$, $\delta^{18}O_p$	0-7	Farrell and Janecek, 1991; Chen et al., 1995
	U1443	5.38°N, 90.36°E	MS, L*, a*, b*	0-3.4	Clemens et al., 2016
	U1445	17.75°N, 84.83°E	TOC, $CaCO_3$, C/N	0-2.3	Lee et al., 2020
	U1446	19.08°N, 85.73°E	$\delta^{18}O_b$, $\delta^{18}O_p$, SST, Rb/Ca	0-1.5	Clemens et al., 2021
	U1447	10.80°N, 93.00°E	MS, L*, a*, b*	0-10	Clemens et al., 2016
	U1448	10.63°N, 93.00°E	MS, L*, a*, b*	0-7	Clemens et al., 2016
Ariabian Sea	722	16.62°N, 59.80°E	$\delta^{18}O_b$, $\delta^{18}O_p$, SST,	0-3.5	Clemens et al., 1996; Herbert et al., 2010
	U1456	16.62°N, 68.84°E	MS, L*	0-10	Pandey et al., 2016
	U1457	17.17°N, 67.93°E	MS, L*	0-10	Pandey et al., 2016
	U1467	4.85°N, 73.28°E	Fe/K, Ca/K	0-2	Betzler et al., 2018; Kunkelova et al., 2018

MS-magnetic susceptibility; $\delta^{13}C_{IC}$-$\delta^{13}C$ of inorganic carbonate; $\delta^{13}C_{OC}$-$\delta^{13}C$ of organic carbonate; BioSi-Biogenic silica; ISM index-Indian summer monsoon index; M_{rs}/MS-ratios of saturation remanence (M_{rs}) to magnetic susceptibility; SST-Sea surface temperature; MS_{FD}-frequency dependent magnetic susceptibility; FeD/FeT-ratios of extractable free Fe_2O_3 to total Fe_2O_3; Hm/Gt-Hematite/Goethite ratio; $\delta^{18}O_b$-$\delta^{18}O$ of benthic foraminifera; $\delta^{18}O_p$-$\delta^{18}O$ of planktonic foraminifera.

Figure captions

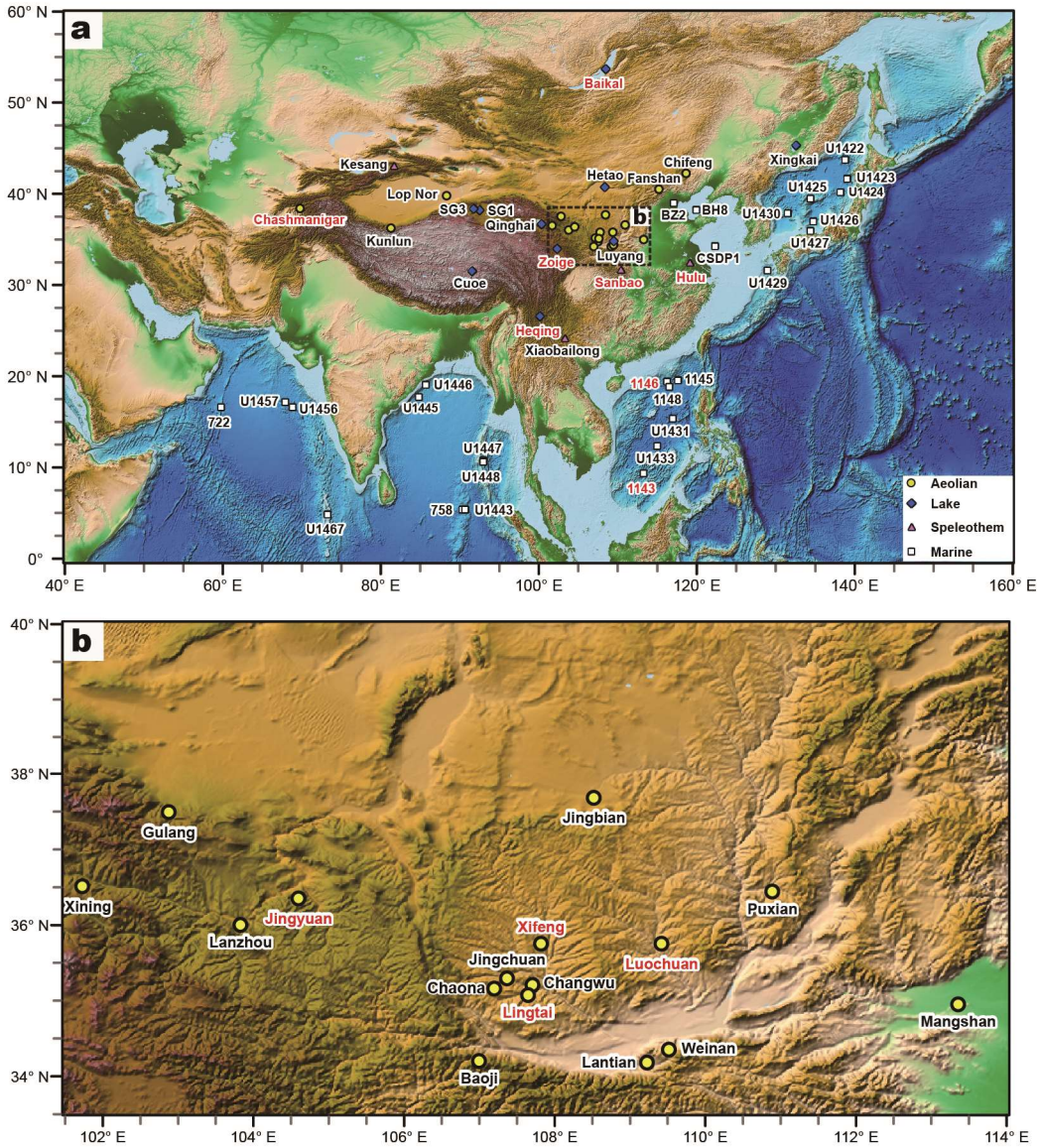

Fig.1. Location of aeolian, lake, speleothem, and marine records in East Asia and its surrounding oceans. Detail information of these sites is presented in Table 1.

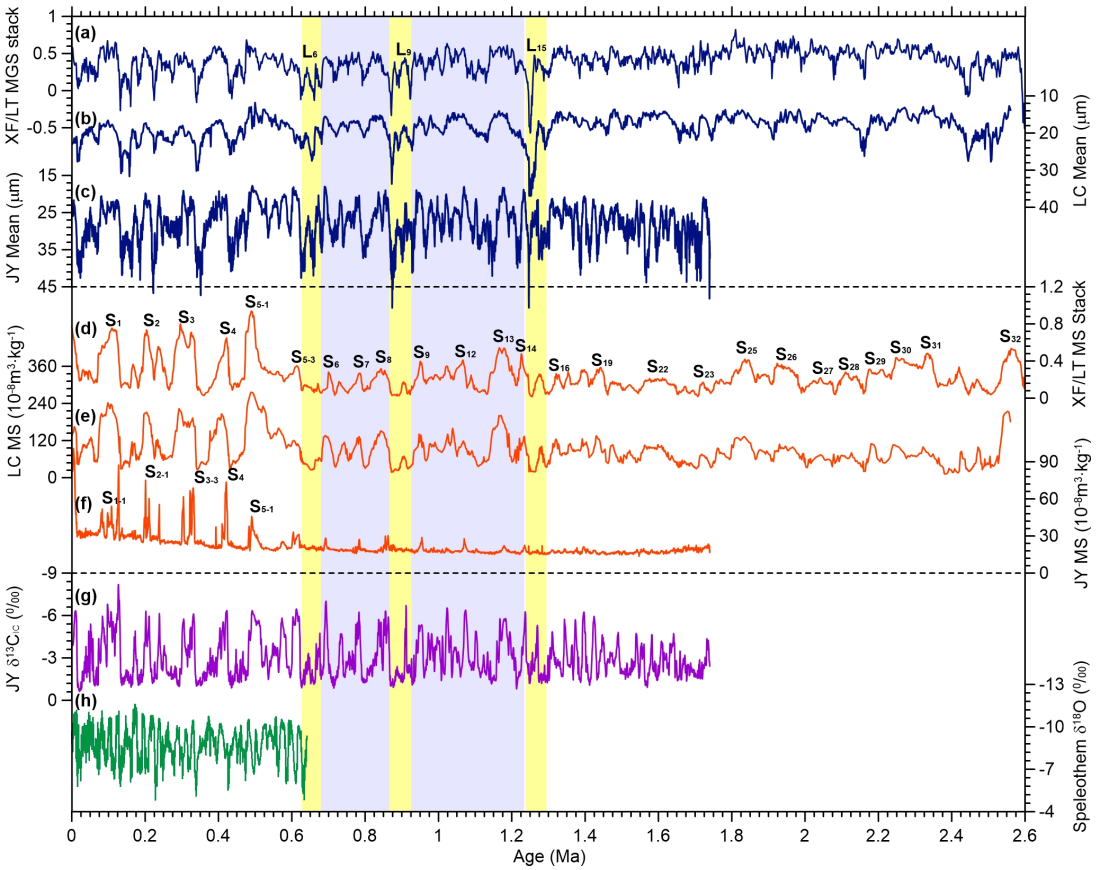

Fig.2. Comparison of loess proxies with speleothem $\delta^{18}O$ record. From top to bottom: (a) Quartz mean grain-size stack (MGS) of Xifeng/Lingtai (XF/LT, Sun et al., 2006a), (b) mean grain size of Luochuan (LC, Han et al., 2020), (c) mean grain size of Jingyuan (JY, Sun et al., 2019), (d) MS stack of XF/LT (Sun et al., 2006a), (e) MS of LC (Han et al., 2020), (f) MS of JY (Sun et al., 2019), (g) $\delta^{13}C_{IC}$ of JY (Sun et al., 2019), and (h) speleothem $\delta^{18}O$ records of Hulu/Sanbao caves (Wang et al., 2001, 2008; Cheng et al., 2016). Light blue bar denotes the Mid-Pleistocene transition, and three yellow bars indicate three loess marker layers of L_6, L_9, and L_{15}.

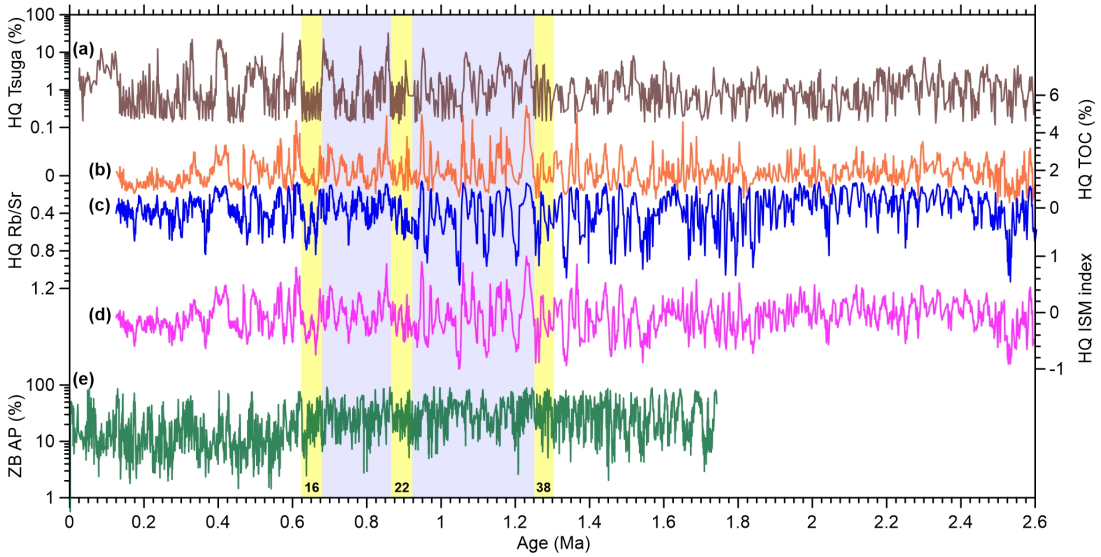

Fig.3. Variations of proxy indicators from Heqing paleolake (HQ) and Zoige Basin (ZB). From top to bottom: (a) *Tsuga* content, (b) TOC, (c) Rb/Sr ratio, and (d) ISM index of HQ paleolake sediments (An et al., 2011); (e) Arboreal pollen abundances (AP%) of ZB sediments (Zhao et al., 2020). Light blue bar denotes the Mid-Pleistocene transition, and three yellow bars indicate three extreme glaciations, corresponding to marine isotope stages (MIS) 16, 22, and 38.

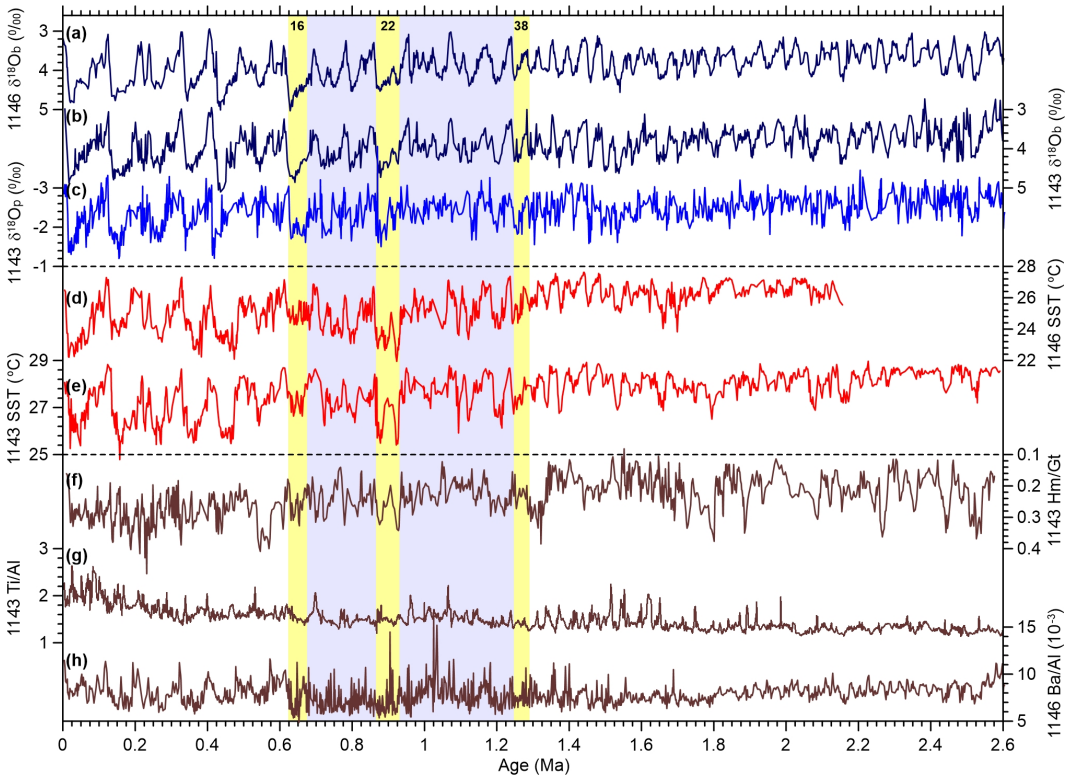

Fig.4. Marine-based proxies of ODP sites 1143 and 1146 from the South China Sea. From top to bottom: (a, b) Benthic $\delta^{18}O$ of ODP sites 1143 (Tian et al., 2002) and 1146 (Clemens et al., 2008), (c) Planktonic $\delta^{18}O$ of ODP site 1143 (Tian et al., 2002), (d, e) Alkenone-based SST records of ODP sites 1146 (Herbert et al., 2010) and 1143 (Li et al., 2011), (f) Hematite/Goethite (Hm/Gt) ratio of ODP site 1143 (Zhang et al., 2009), (g) Ti/Al ratio of ODP site 1143 (Tian et al., 2011), and (h) Ba/Al ratio of ODP site 1146 (Clemens et al., 2008). Light blue bar denotes the Mid-Pleistocene transition, and three yellow bars indicate three extreme glaciations, corresponding to marine isotope stages (MIS) 16, 22, and 38.

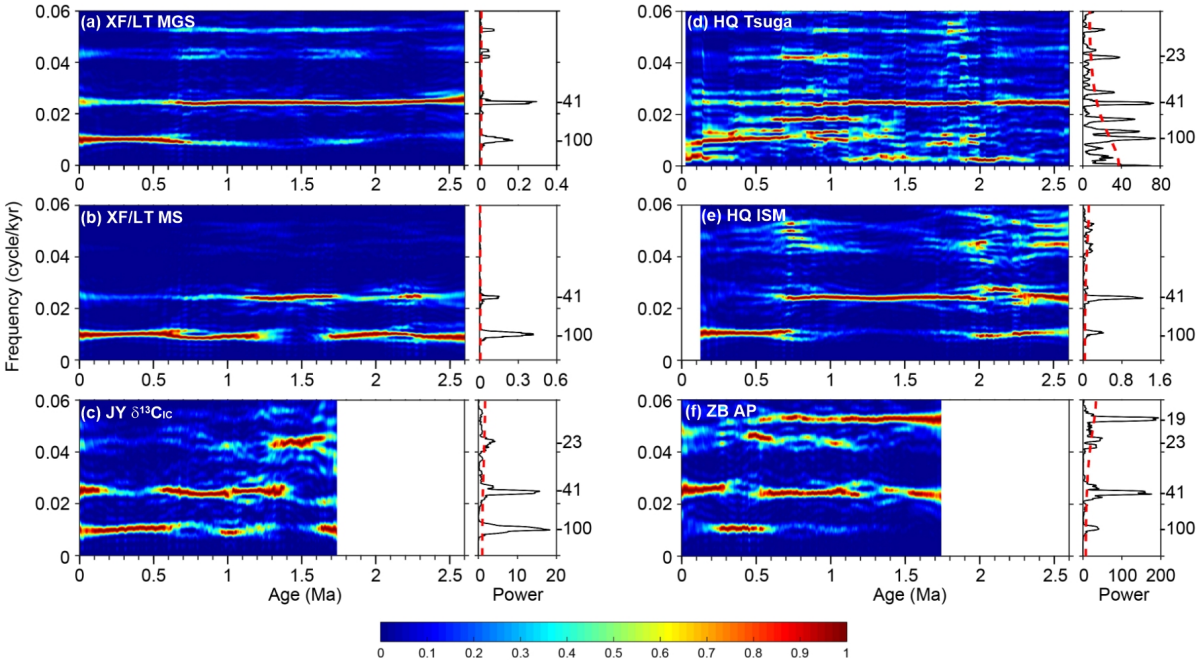

Fig.5. Wavelet and power spectra of six land-based proxies. Left panel (a-c): MGS and MS of XF/LT (Sun et al., 2006a), JY $\delta^{13}C_{IC}$ (Sun et al., 2019); Right panel (d-f): HQ Tsuga content and ISM index (An et al., 2011), ZB AP abundance (Zhao et al., 2020). These data sets were preprocessed to isolate the 100-, 41-, and 21-kyr components using band-passing filters with central frequencies of 0.001, 0.025, and 0.05/kyr and bandwidths of 0.0002, 0.005, and 0.01/kyr before performing the spectral analyses. Red dashed lines in the power spectra indicate 95% confidence level.

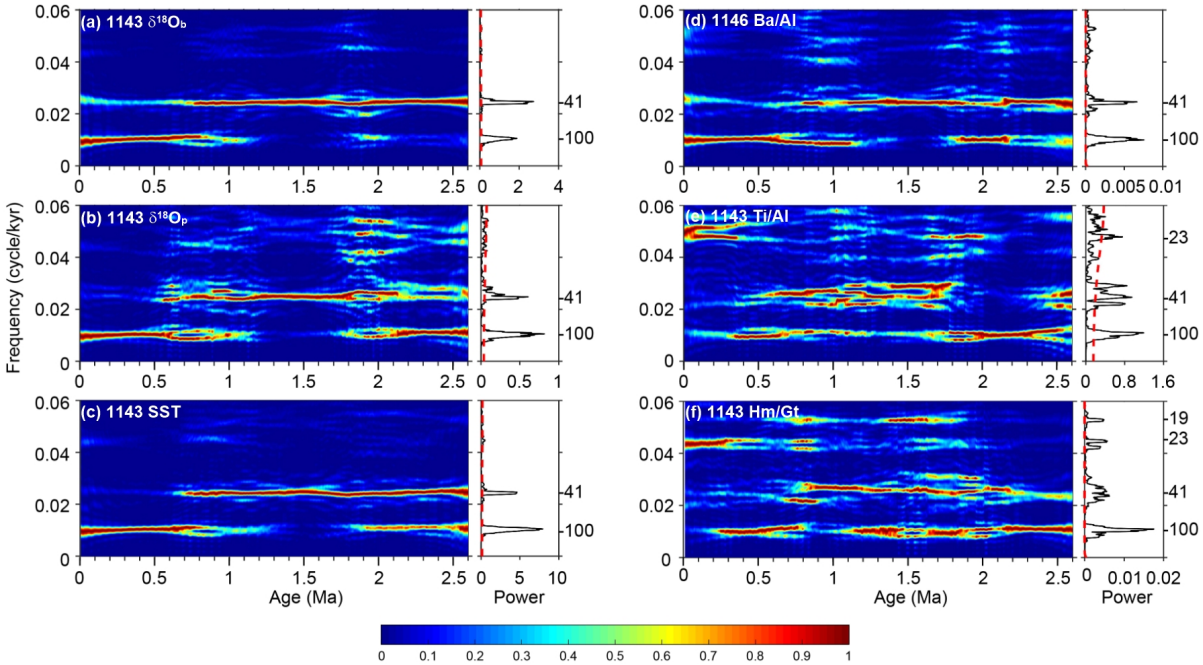

Fig.6. Wavelet and power spectra of six marine-based proxies. Left panel (a-c): $\delta^{18}O_b$, $\delta^{18}O_p$, and SST of ODP site 1143 (Tian et al., 2002; Li et al., 2011); Right panel (d-f): Ba/Al ratio of ODP site 1146 (Clemens et al., 2008), Ti/Al and Hm/Gt ratios of ODP site 1143 (Zhang et al., 2009; Tian et al., 2011). Data sets were preprocessed to isolate the 100-, 41-, and 21-kyr components before performing the spectral analyses. Red dashed lines in the power spectra indicate 95% confidence level.

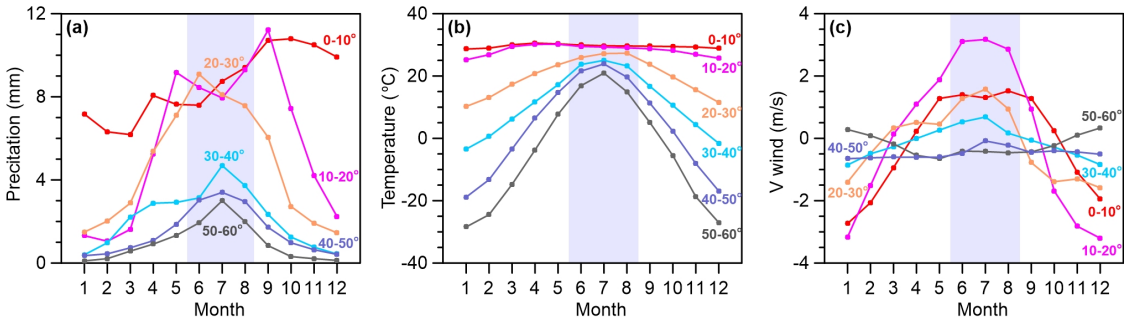

Fig.7. Seasonal cycles of (a) precipitation, (b) temperature, and (c) southerly wind (V wind) over six latitudinal zones (0-60ºN, 105-120ºE) over East Asia in the HadCM3 pre-industrial simulation.

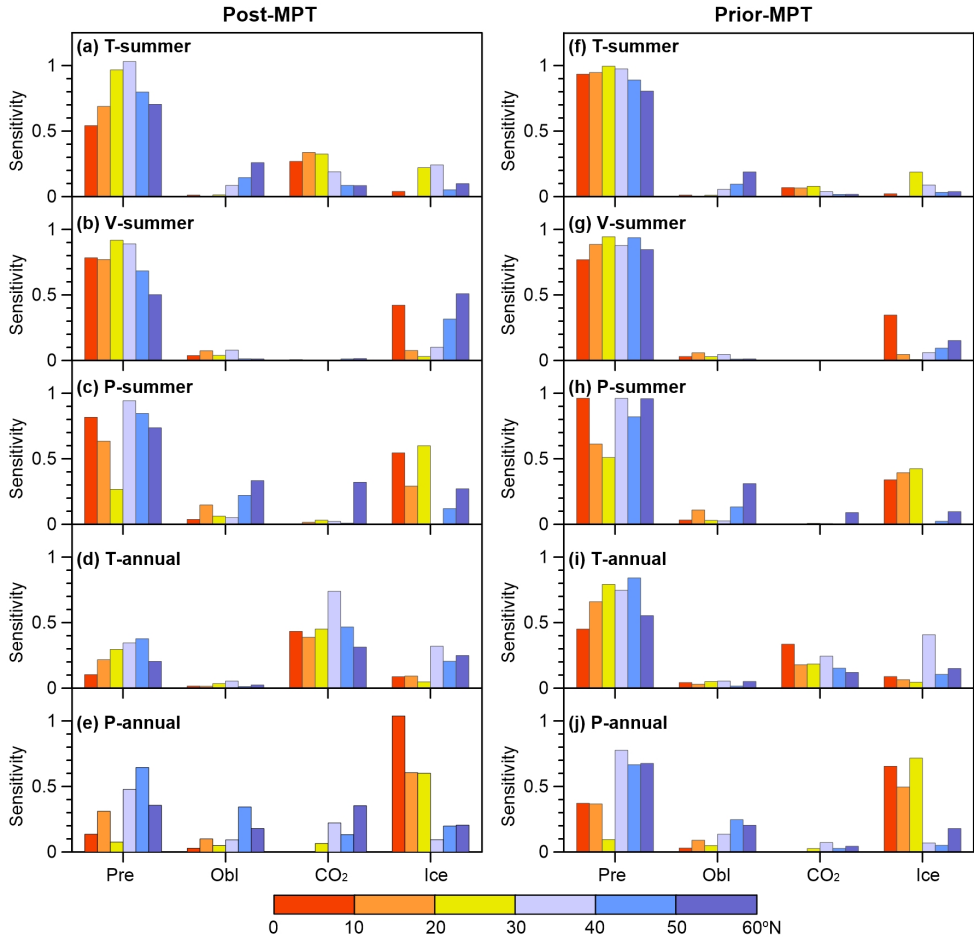

Fig.8. Sensitivity of five climate variables to precession, obliquity, CO_2, and ice forcing. Left paneal (a-e): sensitivities of summer temperature, summer southerly wind, summer precipitation, annual Temperature, and annual precipitation over six latitudinal zones (0-60º N) in East Asia after the MPT (Post-MPT); Right panel (f-j): sensitivities of these variables before the MPT (Prior-MPT).

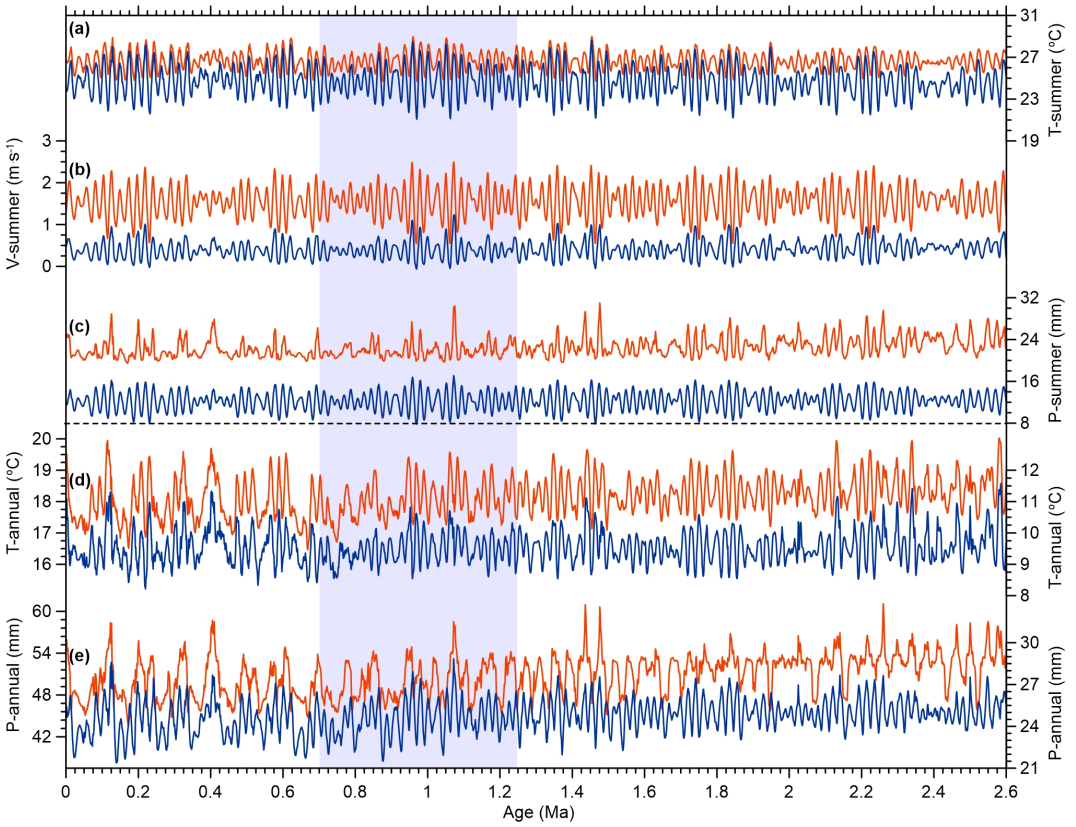

Fig.9. Simulated summer (a-c) and annual (d,e) changes in temperature, southerly wind and precipitation over north (blue lines, 30-40° N) and south China (red lines, 20-30° N).

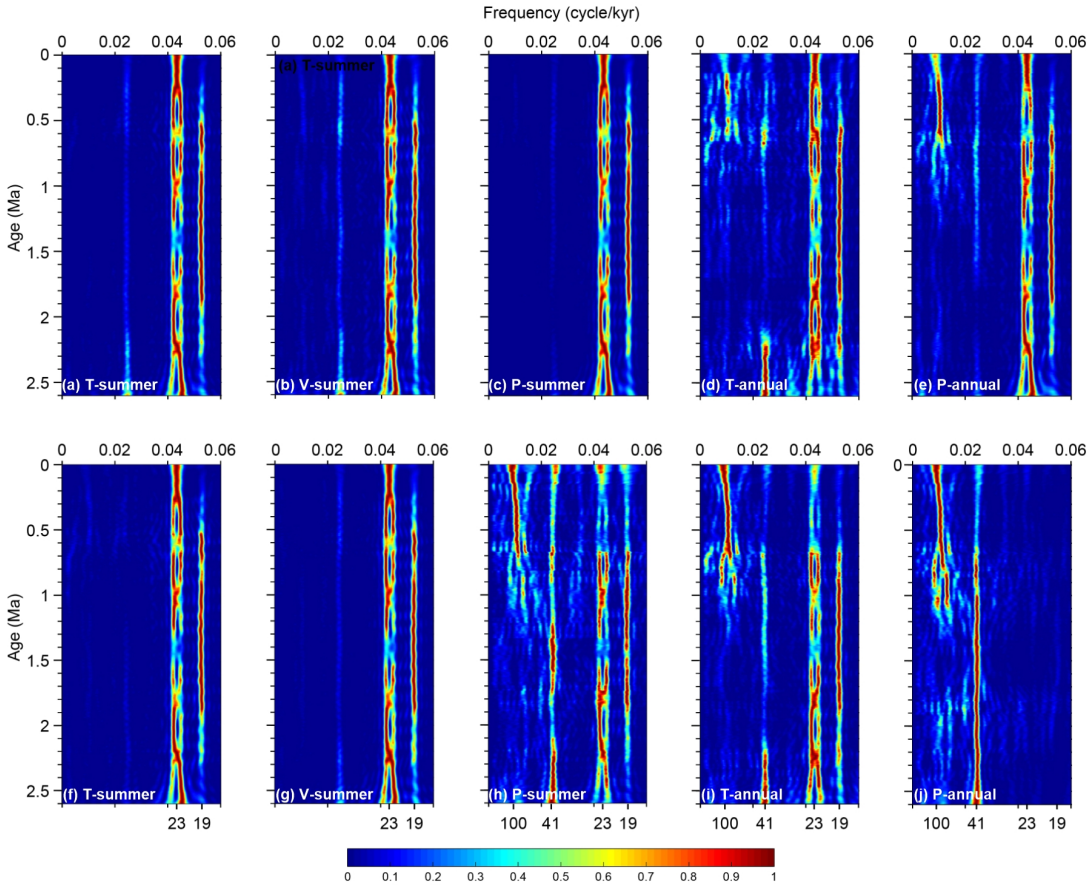

Fig.10. Wavelet spectra of six simulated climate variables over north (upper panel, 30-40° N) and south (lower panel, 20-30° N) China. From left to right: (a, f) summer termperature, (b, g) summer southerly wind, (c, h) summer precipitation, (d, i) annual temperature, and (e, j) annual precipitation.

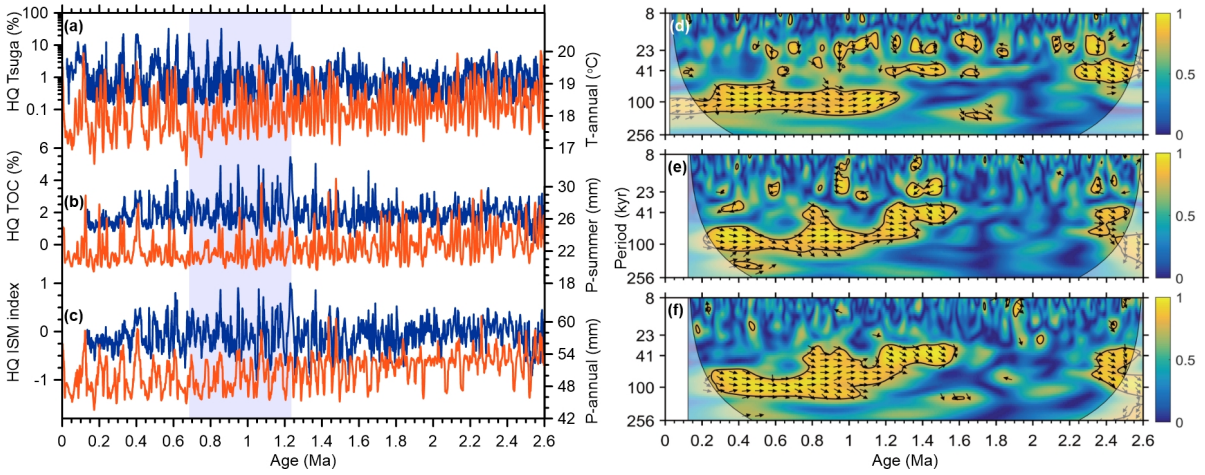

Fig.11. Comparison of simulated temperature and precipitation changes (red lines) at 20-30ºN with three proxies (blue lines, An et al., 2011) from HQ Paleolake and their corresponding wavelet coherence spectra. (a, d) annual temperature vs. *Tsuga* content, (b, e) summer precipitation vs. TOC content, and (c, f) annual precipitation vs. ISM index.

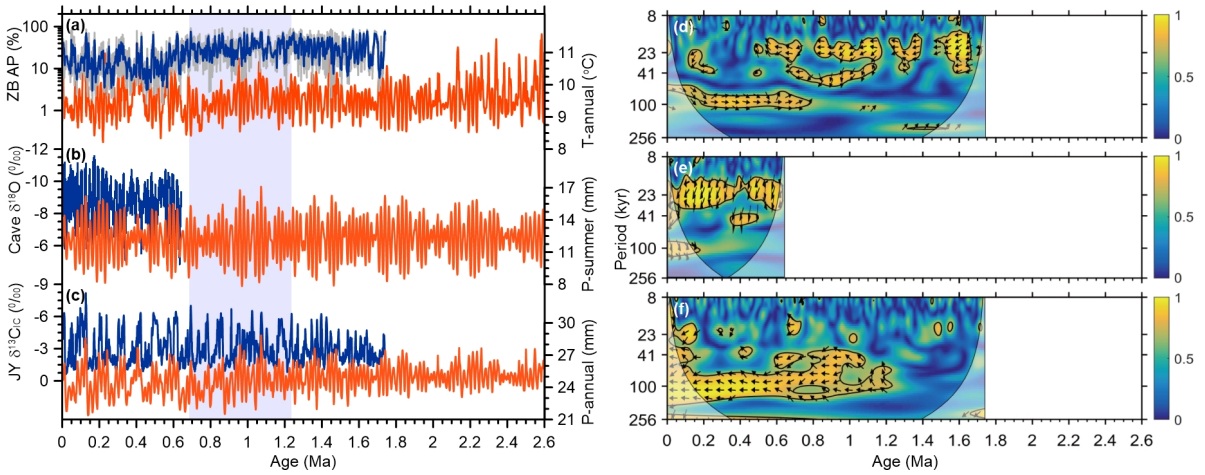

Fig.12. Comparison of simulated temperature and precipitation changes (red lines) with proxy indicators (blue lines) from 30-40ºN and their corresponding wavelet coherence spectra. (a, d) annual temperature vs. AP% (11-points smoothing) from the Zoige basin (Zhao et al., 2020), (b, e) summer precipitation vs. $\delta^{18}O$ from the Hulu/Sanbao caves (Wang et al., 2008; Cheng et al., 2016), and (c, f) annual precipitation vs. $\delta^{13}C_{IC}$ from the JY loess (Sun et al., 2019).